Published in final edited form as:

Inorg Chem. 2023 August 28; 62(34): 14010–14027. doi:10.1021/acs.inorgchem.3c02048.

Electronic structures of nickel(II)-bis(indanyloxazoline)-dihalide catalysts: Understanding ligand field contributions that promote C(sp^2)–C(sp^3) cross-coupling

Brendon J. McNicholas[†,1], **Z. Jaron Tong**[†,2], **Daniel Bím**[1], **Raymond F. Turro**[2], **Nathanael P. Kazmierczak**[1], **Jakub Chalupský**[3,4], **Sarah E. Reisman**[2], **Ryan G. Hadt**[1,*]

[1]Division of Chemistry and Chemical Engineering, Arthur Amos Noyes Laboratory of Chemical Physics, California Institute of Technology, Pasadena, California 91125, United States

[2]Division of Chemistry and Chemical Engineering, The Warren and Katherine Schlinger Laboratory for Chemistry and Chemical Engineering, California Institute of Technology, Pasadena, California 91125, United States

[3]J. Heyrovský Institute of Physical Chemistry, The Czech Academy of Sciences, Dolejškova 3, Prague 8, Czech Republic

[4]Institute of Organic Chemistry and Biochemistry, Academy of Sciences of the Czech Republic, Flemingovo náměstí 2, 166 10 Prague 6, Czech Republic

Abstract

Ni^{II}(IB) dihalide [**IB** = (3a*R*,3a'*R*,8a*S*,8a'*S*)-2,2'-(cyclopropane-1,1-diyl)bis(3a,8a-dihydro-8*H*-indeno[1,2-*d*]-oxazole)] complexes are representative of a growing class of first-row transition metal catalysts for the enantioselective reductive cross-coupling of C(sp^2) and C(sp^3) electrophiles. Recent mechanistic studies highlight the complexity of these ground state cross-couplings, but also illuminate new reactivity pathways stemming from one-electron redox and their significant sensitivities to reaction conditions. For the first time, a diverse array of spectroscopic methods coupled to electrochemistry has been applied to Ni^{II}-based pre-catalysts to evaluate specific ligand field effects governing key Ni-based redox potentials. We also experimentally demonstrate DMA solvent coordination to catalytically-relevant Ni complexes. Coordination is shown to favorably influence key redox-based reaction steps and prevent other deleterious Ni-based equilibria. Combined with electronic structure calculations, we further provide a direct correlation between reaction intermediate frontier molecular orbital energies and cross-coupling yields. Considerations developed herein demonstrate the use of synergic spectroscopic and electrochemical methods to provide concepts for catalyst ligand design and rationalization of reaction condition optimization.

[*]Corresponding Author: rghadt@caltech.edu.
[†]Co-first author

Supporting Information

The Supporting Information is available free of charge on the ACS Publications website at DOI: Materials and methods, NMR spectra, additional UV-vis-NIR, CD, and MCD spectra, additional voltammetry and spectroelectrochemistry data, X-ray crystallographic parameters, and DFT and CASSCF/CASPT2 input parameters and results.

Graphical Abstract

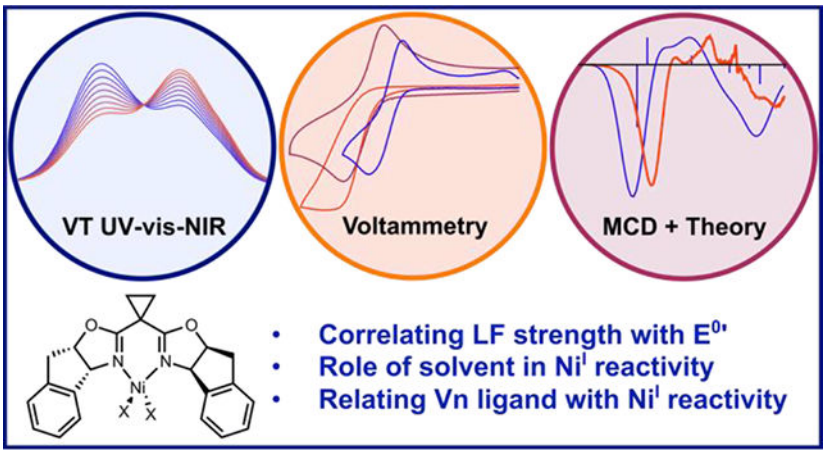

1. Introduction

The number of accessible oxidation states and the possibility of both one- and two-electron redox reactions make nickel a well-suited alternative to precious metals such as iridium and platinum for cross-coupling catalysis. Since the first report of reductive coupling of aryl halides to biaryl products by bis(1,5-cyclooctadiene)nickel^0 in 1971,[1] numerous reports of coupling reactions, including enantioselective cross-coupling, have appeared.[2] Early studies used electrochemistry to render these reactions catalytic in nickel,[3] and in 2007 Durandetti *et al.* demonstrated that elemental manganese could be used as the terminal reductant for the Ni(bipyridine)Br_2-catalyzed reductive cross-coupling of iodobenzene with α-chloroesters in up to 87% yield.[4] The first highly selective enantioconvergent reductive cross-coupling was reported by one of our groups in 2013.[5] Using bis(4-phenyloxazoline) (PhBOX), elemental manganese, and a 30% DMA/THF solvent mixture, high yields and enantioselectivity were obtained for cross-coupling of acyl chlorides and benzyl chlorides. Following this, a variety of chiral ligand frameworks were shown to be effective for the reductive cross-coupling of different electrophile pairs.[2] For example, bis(indanyloxazoline) (Scheme 1, bottom, **IB**) Ni complexes catalyze a variety of reductive alkenylation reactions, including formation of enantioenriched allylic silanes and alkenes with aryl-substituted tertiary stereogenic centers (Scheme 1, bottom).[6,7] More recently, one of our groups has also demonstrated electrocatalytic competency of these Ni^{II} complexes for cross-coupling reactions.[8]

A fundamental and detailed description of both the ground- and excited-state electronic properties of transition metal complexes can help infer catalytic operativity and competency. For example, one of our groups has recently provided detailed electronic structural and mechanistic studies of the ground- and excited-state properties of low-spin Ni^{II} bipyridine aryl halide complexes and their Ni^{I} photogenerated intermediates. These studies identified key structure-function relationships relevant for excited state bond homolysis and oxidative addition reactivity, which allowed for the mechanistic analysis of Ni^{I}-mediated activation of strong C(sp^2)–Cl bonds.[9,10] Our groups also recently participated in collaborative work that utilized cyclic voltammetry under catalytic conditions and UV-vis-

NIR spectroelectrochemistry to better understand the interplay of Ni and Cr oxidation states for Nozaki-Hiyama-Kishi coupling.[11] Another study by Neidig *et al.* utilized a combination of Mössbauer spectroscopy, magnetic circular dichroism, and computations to demonstrate that the kinetic competency of four-coordinate organoiron toward halogen abstraction is dependent on the accessibility and relative energy of iron-based orbitals.[12]

Despite the rapidly growing number of Ni-catalyzed reductive cross-coupling reactions being developed, there have been relatively few detailed mechanistic studies, particularly of bis(oxazoline) Ni complexes. Additionally, although solvent typically has a profound influence on the yield and selectivity of these reactions,[13–18] the influence of solvent coordination to the active catalyst has not been thoroughly studied. A previous study has crystallographically characterized a five-coordinate, DMSO-bound Ni^{II} phenanthroline complex, also suggesting the potential influence of solvent in the catalytic cycle.[19] A recent study by Diao *et al.* has suggested a $Ni^{I/III}$ redox cycle and radical formation and capture are pertinent for catalysis by (biOx)Ni^{II}ArX catalysts, which revised previous suggestions of involvement of $Ni^{0/II}$ oxidation states.[20] In general, uncertainty still exists regarding how the specific ligand, as well as the potential role of solvent coordination, influence both low-spin and high-spin Ni^{II} cross-coupling catalysis.

To this end, we provide the first comprehensive spectroscopic and electrochemical investigation of two reductive cross-coupling catalysts, **Ni^{II}(IB)Cl_2** and **Ni^{II}(IB)Br_2** [**IB** = (3a*R*,3a'*R*,8a*S*,8a'*S*)-2,2'-(cyclopropane-1,1-diyl)bis(3a,8a-dihydro-8*H*-indeno[1,2-*d*]-oxazole)], to provide broad insight into the complex conditions and mechanism (Scheme 1). Although studies related to these complexes by one of our groups were primarily in the context of developing reductive alkenylation, we note that these and similar complexes have also been reported for a number of other reactions, including reductive arylation, 1,2-alkynylboration, and 1,2-vinylboration, further motivating their detailed experimental and computational investigation.[21–31] Here we use variable-temperature (VT) UV-vis-NIR absorption, circular dichroism (CD), vibrational CD (VCD), and magnetic CD (MCD) spectroscopies, coupled with cyclic voltammetry, spectroelectrochemistry, and DFT/TDDFT and multi-reference (CASSCF/CASPT2) calculations to elucidate specific electronic structure contributions to reactivity, as well as the influence of solvent on the efficacy of catalytic transformations (Scheme 1). Quantifying halide-dependent spectral features directly connects ligand field strength and redox potentials. Similarly, studying three solvents with different donor numbers (DNs) provides a route toward understanding previously reported empirical solvent optimization studies. We demonstrate that DMA solvent can coordinate to catalytically-relevant Ni species and evaluate the potential role of solvent coordination in their reactivity. Based on previously reported yields and findings reported here, we suggest solvent coordination and low temperature can favorably influence driving forces and kinetic barriers of key reaction steps leading to cross-coupled product. These studies provide new insights relevant to the catalytic reactivity of chiral bis(oxazoline) Ni catalysts that have been recently popularized for a variety of asymmetric Ni-catalyzed cross-coupling reactions (Scheme 1).

2. Results and Analysis

2.1 Room-Temperature UV-Vis-NIR, CD, and MCD Characterization of $Ni^{II}(IB)Cl_2$ and $Ni^{II}(IB)Br_2$ in a Non-Coordinating Solvent

Due to the absence of low-energy charge transfer bands in the UV-vis-NIR, electronic absorption spectra of **$Ni^{II}(IB)Cl_2$** and **$Ni^{II}(IB)Br_2$** in DCM (donor number, DN = 2.4)[32,33] (Figures 1A–C and 1D–F, respectively) provide rich insights into the Ni^{II} ligand field through observation of numerous spin-allowed and spin-forbidden ligand field transitions (Table 1). These transitions arise from the orbital triplet ground state (i.e., $^3T_1(F)$ in an idealized T_d geometry) of the S = 1 d^8 Ni^{II} complexes and exhibit correspondingly weak molar absorptivities at 294 K. CD and MCD spectroscopies provide complementary, signed, spectroscopic methods to resolve overlapping ligand field transitions. Due to the presence of the chiral **IB** ligand, the Ni^{II}-based ligand field transitions exhibit CD intensity (Figures 1B and 1E), and both complexes exhibit room temperature MCD signals at 1.4 T (Figures 1C and 1F, respectively). A detailed discussion of band assignments can be found in Supporting Information Section S3.

The ligand field transitions of **$Ni^{II}(IB)Cl_2$** relative to **$Ni^{II}(IB)Br_2$** are blueshifted by ~120 – 710 cm^{-1} in DCM (overlaps in Figure S17), consistent with stronger donation from chloride relative to bromide. To estimate the relative ligand field strengths, we average the assigned spin-allowed transitions (bands 1 – 7). Doing so provides relative ligand field strengths of ~12 365 cm^{-1} and ~11 975 cm^{-1} (Δ = ~390 cm^{-1}) for **$Ni^{II}(IB)Cl_2$** and **$Ni^{II}(IB)Br_2$**, respectively, in accord with the greater ligand field strength in the chloride complex relative to bromide. As will be shown below, the ligand field bands and ligand field strengths can be directly related to the energies of the Ni^{II}-based redox active molecular orbitals (RAMOs) and, thus, complex redox potentials (*vide infra*, Section 3.3). To the best of our knowledge, this provides the first experimental connection between ligand field spectroscopy and the electrochemical potentials of Ni^{II}-based enantioselective cross-coupling catalysts.

2.2 Vibrational CD Spectroscopy of $Ni^{II}(IB)Cl_2$ and $Ni^{II}(IB)Br_2$

Pseudo-T_d Ni(II)/Co(II) and pseudo-O_h V(III) complexes can exhibit large splittings of their orbital triplet ground states. These splittings can be observed using techniques such as electronic Raman or VCD. The latter is the infrared analogue of electronic CD spectroscopy and provides a means to determine absolute stereochemical configurations or probe low-energy electronic transitions in chiral transition metal complexes.[34,35] VCD signals are observed for both **$Ni^{II}(IB)Cl_2$** and **$Ni^{II}(IB)Br_2$** complexes dissolved in d^2-DCM (Figure 2). Note high sample concentrations are necessary for VCD measurements. Despite substantial trimerization of **$Ni^{II}(IB)Cl_2$** at these concentrations (*vide infra*, Section 2.4), the observed VCD transition is still assigned to the four-coordinate species, as evidenced by calculations (Figure S121) and spectral consistency with the **$Ni^{II}(IB)Br_2$** analogue, which does not undergo trimerization at high concentrations in DCM. Furthermore, to confirm the observed VCD spectral intensity for **$Ni^{II}(IB)X_2$** complexes corresponds to a ligand field transition, the d^{10} complex, **$Zn^{II}(IB)Cl_2$**, was synthesized in a manner analogous to the Ni^{II} complexes. Note that an analogous complex, $Cu^{II}(IB)Cl_2$, has been previously reported.[36] The VCD spectrum of **$Zn^{II}(IB)Cl_2$** in d^2-DCM does not exhibit electronic absorption in the region

of 1800 – 3200 cm^{-1} (Figure 2). **$Ni^{II}(IB)Cl_2$** exhibits a moderately sharp (FWHM = ~730 cm^{-1}) ligand field transition at ~2170 cm^{-1}, while **$Ni^{II}(IB)Br_2$** exhibits a transition (FWHM = ~970 cm^{-1}) at ~2210 cm^{-1}. For both complexes, this band (band 1, $^3B_1(F) \rightarrow {}^3A_2$ transition in C_{2v}) arises from a transition within the orbital triplet ground state ($^3T_1(F)$ in T_d), which is split by low symmetry distortions and spin-orbit coupling. Note the positive sign of the VCD band is consistent with the other $^3A_2$ states observed with CD (Figure 1B and 1E). While the relative ground state splittings are quite similar between the two complexes, the small increase in splitting for **$Ni^{II}(IB)Br_2$** is likely due to the greater spin-orbit coupling constant for Br relative to Cl.

This application of VCD determines electronic excited state energies of the low-symmetry split orbital triplet ground state of transition metal-based enantioselective cross-coupling catalysts for the first time. These data, combined with the UV-vis-NIR, electronic CD, and MCD data, have allowed for the experimental determination of a complete ligand field energy level diagram for the **$Ni^{II}(IB)X_2$** complexes. All transitions to individual excited states in T_d and C_{2v} symmetry are assigned in the correlation diagram in Figure 3.

2.3 Room Temperature UV-Vis-NIR, CD, and MCD Characterization of $Ni^{II}(IB)Cl_2$ and $Ni^{II}(IB)Br_2$ in Coordinating Solvents

To complement data obtained in DCM (poor σ and π donor) and to assess the solvent-dependent behavior of **$Ni^{II}(IB)X_2$** complexes, room temperature UV-vis-NIR absorption, CD, and 1.4 T MCD spectra were also acquired in MeCN (moderate σ donor and moderate π acceptor) and DMA (very strong σ donor and moderate π acceptor). These solvents were selected for their relative differences in dielectric constant and Lewis basicity/acidity to assess the effects of solvent environment on geometric and electronic structure, which can subsequently be correlated with catalytic activity and selectivity.

UV-vis-NIR spectra of **$Ni^{II}(IB)Cl_2$** and **$Ni^{II}(IB)Br_2$** exhibit significant solvent dependence (Figures S9 and S10). In addition to decreased overall intensities compared to transitions observed in DCM, new spectral intensity grows in at ~23 000 cm^{-1}, with weak intensity in MeCN and greatest intensity in DMA. These spectral changes are also manifested in the solvent-dependent CD and MCD spectra (Figures S44–S47), with the new spectral intensity at ~23 000 cm^{-1} corresponding to a new negative band in CD and MCD. As demonstrated in Section 2.4 below, this new band reflects an equilibrium between the four- and five-coordinate, solvent coordinated species. Thus, electronic spectroscopies provide a direct handle on DMA coordination to Ni^{II} dihalide complexes relevant to catalysis.

2.4 Variable-Concentration and Variable-Temperature UV-Vis-NIR Spectroscopy of $Ni^{II}(IB)Cl_2$ and $Ni^{II}(IB)Br_2$

Solvent and additive evaluation are necessary steps in the optimization of transition metal-catalyzed organic reactions. However, these steps can be somewhat arbitrary and rely on a large empirical screening matrix. Previous studies of **$Ni^{II}(IB)X_2$** demonstrated catalytic yields are maximized in DMA and when the reaction is cooled to 0–5 °C.[6–8] By obtaining VT UV-vis-NIR spectra for both **$Ni^{II}(IB)Cl_2$** and **$Ni^{II}(IB)Br_2$** in DCM and DMA, we

aimed to provide insight into precatalyst speciation and, in turn, to provide experimental thermodynamic data for rational catalyst and condition design.

As the concentration of **$Ni^{II}(IB)Cl_2$** is increased in DCM, a noticeable color change from pink to orange is observed. Correspondingly, new electronic absorption bands are observed at 13 100 cm^{-1} and 22 840 cm^{-1} with increasing concentration (Figure S16). These additional absorption bands are ascribed to the formation of a **$[Ni^{II}(IB)Cl_2]_3$ μ-Cl** trimer. A previously obtained crystal structure of this species shows it possesses both five- and six-coordinate formal Ni^{II} centers.[37]

The UV-vis-NIR spectra of **$Ni^{II}(IB)Cl_2$** in DCM (4.3 mM) and DMA (3.6 mM) also depend on temperature (Figure 4A and 4B). Because of the number of overlapping transitions present in each spectrum, the VT spectra were resolved using global modeling of the temperature dependence through nonlinear regression at multiple wavelengths and bootstrapping (Figures S13–S15).[38,39] In DMA, the VT UV-vis-NIR spectra reflect an equilibrium between the four- and five-coordinate, DMA coordinated species for **$Ni^{II}(IB)Cl_2$** (five-coordinate absorption maximum at 22 840 cm^{-1}) and **$Ni^{II}(IB)Br_2$** (five-coordinate absorption maximum at 23 230 cm^{-1}). In DCM, the VT UV-vis-NIR spectra reflect an equilibrium between a monomeric and trimeric form (trimer absorption maxima at 22 840 cm^{-1} and 20 160 cm^{-1}). We note the excellent agreement between the resolved spectra of the four-coordinate species and the spectra of isolated **$Ni^{II}(IB)Cl_2$** and **$Ni^{II}(IB)Br_2$** obtained in DCM (Figure 4 and S12). In contrast to **$Ni^{II}(IB)Cl_2$**, **$Ni^{II}(IB)Br_2$** exhibited no trimerization up to 152.1 mM or in VT studies down to –85 °C (Figures S18–S19).

In addition to resolving the spectra for four-coordinate, five-coordinate, and trimeric species, these fits provide thermodynamic parameters based on the two equilibrium expressions,

$$K_{eq} = \frac{[(Ni(IB)X_2)_3]}{[Ni(IB)X_2]^3}, \; K_{eq} = \frac{[Ni(Solv.)(IB)X_2]}{[Ni(IB)X_2]} \quad (1)$$

K_{eq} values for DMA coordination to **$Ni^{II}(IB)Cl_2$** and **$Ni^{II}(IB)Br_2$** are similar (0.58 and 0.97, respectively, Table 2). Furthermore, $K_{eq} = 16.7$ is calculated at 294 K for formation of the **$[Ni^{II}(IB)Cl_2]_3$ μ-Cl** trimer in DCM. Despite the exergonicity of this process (Table 2), the extent of reaction is only 0.09% at 4.3 mM, which is why essentially no trimer is observed at room temperature at low Ni^{II} concentrations. As expected for associative reactions, all entropy values for solvent coordination and trimerization are negative. Note that the extent of temperature-dependent reaction is primarily sensitive to the ratio of the enthalpy to entropy, and the global fitting can extract this value with <1% uncertainty. However, global fitting can additionally extract the absolute standard enthalpies and entropies, albeit with higher uncertainty. From K_{eq} values, we estimate concentrations of ~37% and ~49% for DMA-coordinated **$Ni^{II}(IB)Cl_2$** (3.6 mM) and **$Ni^{II}(IB)Br_2$** (3.5 mM), respectively, at 294 K. Upon cooling to 273 K, these values increase significantly to ~53% and ~69%, respectively.

As depicted in Figure 5, the preceding analysis provides the first detailed view of the effects of dielectric constant, concentration, and solvent donicity on the speciation equilibria of Ni^{II} precatalyst solutions. With high solvent donicity, the equilibrium shifts toward a five-coordinate, solvent coordinated species for both **$Ni^{II}(IB)Cl_2$** and **$Ni^{II}(IB)Br_2$**. Increasing concentration and low dielectric constant shifts the equilibrium toward a trimeric species for **$Ni^{II}(IB)Cl_2$**. Thus, solvent coordination, temperature, and catalyst concentration are important effects that contribute to catalyst speciation and activity under reaction conditions (*vide infra*, **Discussion**). VT spectroscopies provide a direct handle on the speciation and the associated thermodynamics.

2.5 Cyclic Voltammetry of $Ni^{II}(IB)Cl_2$ and $Ni^{II}(IB)Br_2$ in DCM, MeCN, and DMA

To assess the effects of solvent donicity and dielectric constant on the electrochemical properties of **$Ni^{II}(IB)X_2$** complexes, scan rate-dependent cyclic voltammetry data were acquired in DCM, MeCN, and DMA (Figure 6 and Figures S48–S59). Table 3 provides peak and formal potentials for initial redox events, while Table S1 provides peak and formal potentials for unique re-oxidation and re-reduction events that result from chemical reactions following initial electron transfers. Additional details and discussions are provided in Supporting Information Section S5.

Previous studies have provided formal potentials for both aromatic and non-aromatic Ni^{II} diimine systems, with many reports providing kinetic analyses with substrate present.[41,20] However, to our knowledge, this is the first example of detailed solvent-dependent electroanalytical chemistry for non-aromatic Ni^{II} cross-coupling catalysts. In general, precatalyst electrochemical responses are remarkably solvent dependent. In all three solvents, **$Ni^{II}(IB)Cl_2$** and **$Ni^{II}(IB)Br_2$** both exhibit single, electrochemically irreversible reduction events with significantly shifted oxidative waves (Figures 6, and S50, S54, S58). The general irreversibility required use of peak potentials ($E_{p,a}$ or $E_{p,c}$), potentials at half of the peak current value ($E_{p/2}$), and inflection potentials (accurate estimate of formal potential, $E^{0'}$) for analysis.[42] Our measured Fc formal potentials in DMA and MeCN are 85 and 91 mV vs 0.01 M $Ag^{+/0}$, respectively, indicating accurate conclusions can be drawn regarding solvent effects on measured formal potentials of the Ni complexes in these solvents. In DCM, the measured Fc formal potential is 215 mV. Therefore, measured formal potentials in DCM will appear negatively shifted relative to values in DMA and MeCN.

Based on shifts in peak potential as a function of scan rate and scan rate normalized voltammetry (current function) in all three solvents (Figures S48–S58), as well as differential pulse voltammetry and variable temperature voltammetry in DMA for **$Ni^{II}(IB)Cl_2$** (Figure S58), we can draw some insightful conclusions regarding the reduction mechanism, as the current function and shift in peak potential are dictated by the particular chemical and electrochemical mechanism. These conclusions also apply to **$Ni^{II}(IB)Br_2$**. We ascribe the reduction of both complexes to a concerted E_qC_i (in DMA and MeCN, solvent coordination and/or halide loss occur in concert) or step-wise E_iC_i mechanism (DCM), where slow electron transfer is followed by rapid halide loss. In DCM, three-coordinate **$Ni^{I}(IB)X$** will be generated upon reduction, with no subsequent solvent coordination. The lack of return current, shift in peak potential as a function of the logarithm of the scan

rate near 29.6 mV, with ~33 mV observed here, and decrease in the current function toward a limiting value as the scan rate is increased supports a kinetically-controlled, stepwise reduction followed by rapid halide loss (Figures S48 and S50). Activation of DCM by other nickel complexes supported by naphthyridine-diimine ligands has been observed previously.[43] However, spectroelectrochemical data obtained in DCM do not support reactivity of the **Ni^{I}(IB)X** with solvent (Figures S73–S75). Overall, this analysis featuring electron transfer coupled to rapid halide loss is consistent with halide dissociation observed previously using extended X-ray absorption fine structure (EXAFS) for a low-spin Ni^{II} biOx aryl halide complex upon reduction with potassium graphite.[20]

Experimental formal potentials for chemically-coupled reduction of **Ni^{II}(IB)Cl$_2$** and **Ni^{II}(IB)Br$_2$** to **Ni^{I}(IB)Cl** and **Ni^{I}(IB)Br** in DCM are −1.47 V and −1.26 V vs. Fc$^{+/0}$, respectively (Table 3). It is therefore ~0.21 V (~1695 cm^{-1}) harder to reduce **Ni^{II}(IB)Cl$_2$** relative to **Ni^{II}(IB)Br$_2$**. This observation is consistent with the energetic shifts in the spin-allowed ligand field bands in DCM in experiment (*vide supra*, Section 2.1) and calculations (*vide infra*, Section 3.2 and 3.3). In MeCN and DMA, **Ni^{II}(IB)Cl$_2$** (Figures S54 and S58) and **Ni^{II}(IB)Br$_2$** (Figure 6, left) both exhibit superficially quasi-reversible voltammetry for the reduction. Experimental formal potentials for chemically-coupled reduction in MeCN/DMA of **Ni^{II}(IB)Cl$_2$** and **Ni^{II}(IB)Br$_2$** are −1.32/−1.47 V and −1.05/−1.23 V vs. Fc$^{+/0}$, respectively (Δ = ~0.27/~0.24 V (~2180/1935 cm^{-1})). Thus, for all solvents used here, it is harder to reduce **Ni^{II}(IB)Cl$_2$** relative to **Ni^{II}(IB)Br$_2$**.

Based on the VT UV-vis-NIR data in DMA (*vide supra*, Section 2.4), both the Ni^{II} four-coordinate and five-coordinate solvent adducts exist in equilibrium, and this can potentially influence the electrochemistry measured in this solvent. One possibility for the reduction mechanism for these species is reduction followed by halide loss and, for the four-coordinate portion of the complex, coordination of DMA to the Ni^{I} center, which could occur in a concerted or stepwise fashion. For a concerted mechanism, the anticipated shift in peak potential as a function of log(v) is 29.6/α mV, where α is the transfer coefficient for electron transfer.[42] Based on the observation of only one differential pulsed voltammetry wave on the forward scan and the shift in peak potential with log(v) (~77–104 mV), we propose that the reduction and chemical follow up reaction in both MeCN and DMA (i.e., solvent coordination at Ni^{I}) is a concerted process. The two return waves observed scanning oxidatively suggest generation of a halide-dissociated species that is re-oxidized at more positive potentials. This conclusion is supported by VT differential pulse voltammetry (Figure S58), where the differential current at the more positive wave decreases as temperature is decreased, while the differential current at the wave ascribed to re-oxidation of five-coordinate Ni^{I} increases. Based on behavior previously observed for these systems and our computed formal potentials,[20] the more positive re-oxidation could arise from re-oxidation of a Ni^{I}/Ni^{I} dimer that forms after the initial reduction. However, we favor the interpretation featuring re-oxidation of the halide-dissociated species based on computed formal potentials (*vide infra*, Section 3.3) and lack of return oxidation near the reduction event in DCM, where Ni^{I} is anticipated to dimerize rapidly. Further supporting our hypothesis, an additional wave near where three-coordinate Ni^{I} is predicted to oxidize is present in MeCN, but not in DMA (Figures S52 and S54), supporting the

weaker coordination affinity of MeCN and our assignment of the species generated upon reduction.

Potentials for chemically-coupled reductions in DMA are more negative relative to MeCN by ~200 mV for both complexes. As discussed further in Section 3.3, this difference is ascribed to DMA being a higher donicity solvent and coordinating to the Ni^{II} center. Note that solvent coordination is not observed in DCM and only weakly so in MeCN. It is further interesting to note that the reduction potential for **Ni^{II}(IB)Cl_2** in both DCM and DMA is −1.47 V vs. $Fc^{+/0}$, respectively; for **Ni^{II}(IB)Br_2**, these are −1.26 V and −1.23 V vs. $Fc^{+/0}$, respectively. The similarity in reduction potentials in DCM and DMA is ascribed to the relative Fc formal potentials in DCM vs. DMA and the role of solvent in facilitating the Ni–X bond rupture upon one-electron reduction, with the anionic halide loss more facile in DMA relative to DCM. Because of these considerations and the electronic structure calculations presented in Section 3.3, the more quantitative comparison of potentials for the reduction with and without coordinated solvent is that between MeCN and DMA. Furthermore, the temperature-dependent cyclic voltammetry demonstrates a negatively shifted reduction potential as the temperature is lowered, which may be due to increasing the relative amount of five-coordinate species. Thus, overall, solvent coordination results in a harder to reduce Ni^{II} center. By extension, this can be further translated to a more reducing Ni^{I} species, which, under catalytic conditions, can facilitate oxidative addition (*vide infra*, **Discussion**).[44]

Ligand field and bonding effects on Ni^{II}-based redox potentials can be further elucidated using electronic structure calculations (*vide infra*, Section 3.3) and through correlations to electronic spectroscopy, as transitions to the RAMO are also observed experimentally. Differences in measured redox potentials correlate directly with specific structural influences on the energy of the RAMO.

Finally, based on the measured formal potentials, proposed electrochemical mechanisms, and additional electronic structure calculations of redox potentials (*vide infra*, Section 3.3), we do not believe **Ni^{0}(IB)X_2** (or Ni^0 in any form) is thermodynamically accessible in the electrochemical window of common electrochemistry solvents, which supports a $Ni^{I/III}$ catalytic cycle for reductive alkenylation and potentially related reactions involving bis(oxazoline)–Ni complexes.[20] No additional reduction beyond Ni^{I} is required for oxidative addition of substrates for which this catalyst has been previously demonstrated to be competent, and this finding has important mechanistic implications for bis(oxazoline)–Ni-catalyzed reactions more generally.

2.6 Spectroelectrochemistry of Ni^{II}(IB)Cl_2 and Ni^{II}(IB)Br_2 in DCM and DMA

To rationalize the noticeable difference in electrochemical response of **Ni^{II}(IB)X_2** in DCM vs. DMA and to further understand the solvent-dependent catalytic activity, time-based spectroelectrochemical measurements were performed for both negative and positive polarizations. These measurements are the first comprehensive solvent-dependent spectroelectrochemistry for Ni^{II} cross-coupling catalysts. All experimental plots are shown in Figures S61–S87. In conjunction with calculations (*vide infra*, Figures S133–S140), we can assign transient spectra to possible species generated under polarized conditions. In

DCM, polarization negative of the first reduction generates a spectrum with a slightly blue-shifted, higher-energy ligand field transition, consistent with calculated spectra for **Ni^{I}(IB)X** (Figures S133 and S135).

Reduction of both **Ni^{II}(IB)Br_2** and **Ni^{II}(IB)Cl_2** in DMA generates spectra consistent with calculated spectra corresponding to a solvent-coordinated Ni^{I} species, **Ni^{I}(IB)(DMA)X** (Figures S134 and S136). All ligand field bands decay in intensity upon oxidation, which is ascribed to oxidative degradation or oligomerization. Spectra obtained after positive polarization of **Ni^{II}(IB)Br_2** are consistent with bromide speciation.[45]

3. Computational Results

In this section, we sought to gain further insights into the electronic structures of the precatalysts by comparing experimental spectra and redox potentials with computed ground- and excited-state properties obtained from a combination of DFT, time-dependent DFT (TDDFT), and multireference CASSCF/CASPT2 calculations. TDDFT and multireference methods predict electronic transitions below ~25 000 cm^{-1} are ligand field excitations, and differences between computed electronic spectra of **Ni^{II}(IB)X_2** complexes arise from differences in ligand field strength. Generally, increased ligand field strength destabilizes the β lowest unoccupied molecular orbitals (β-LUMOs), which negatively shifts the reduction potential of **Ni^{II}(IB)Cl_2** relative to **Ni^{II}(IB)Br_2**. DFT calculations also corroborate that, depending on reaction conditions (such as the choice of coordinating/non-coordinating solvent or Ni^{II} concentration), precatalysts can exist in complex equilibria featuring four-coordinate **Ni^{II}(IB)X_2**, five-coordinate **Ni^{II}(IB)(solv.)X_2**, or trimeric **[Ni^{II}(IB)X_2]$_3$ μ-X** species. Finally, we demonstrate the role of ligand–metal covalency in tuning the relative reactivity of the catalyst resting state; the bonding of this species further manifests in a correlation between reaction yield and its oxidation potential relative to those of $C(sp^3)$ radicals.

3.1 DFT and TDDFT Calculated Thermodynamics and Spectra of Ni^{II}(IB)Cl_2 and Ni^{II}(IB)Br_2 Precatalysts

Using a TPSSh functional with a conductor-like polarizable continuum model (CPCM) (see Computational Details in Section S8 of the Supporting Information), the ground state wave functions of **Ni^{II}(IB)Cl_2** and **Ni^{II}(IB)Br_2** are high-spin ($S = 1$) Ni^{II}. TDDFT was used to calculate the electronic transition energies (Table 4). The intensities of the lower-energy ligand field bands are underestimated relative to experiment and do not contribute significantly to the overall predicted spectra (Figures S92–S93). Additionally, two-electron excitations and spin-flip transitions are inaccessible through conventional TDDFT and, thus, are not observed in the spectral predictions (e.g., $^3A_2$(F), band 4 and $^1T_2/^1E$, band i excited states in T_d). For d^8 Ni^{II}, there are only six spin-allowed ligand field transitions accessible using TDDFT (Table 4). Therefore, full assignment of all absorption bands from Section 2.1 cannot be achieved using this approach. A more detailed analysis must be obtained from the multi-reference CASSCF/CASPT2 calculations (*vide infra*, Section 3.2). Nonetheless, qualitative correlations can be made by comparing to assignments in the parent T_d point group (Table 4). While the absolute calculated energies of the ligand

field transitions are not well-reproduced with TDDFT, the average energies agree well with the experimentally determined relative ligand field strengths (*vide supra*, Section 2.1). For example, experimental values of ~12 365 cm^{-1} and ~11 975 cm^{-1} (Δ = ~390 cm^{-1}) were determined for **Ni^{II}(IB)Cl_2** and **Ni^{II}(IB)Br_2**, respectively, and are computationally estimated to be ~13 780 cm^{-1} and ~13 370 cm^{-1} (Δ = ~410 cm^{-1}).

In addition to correlating TDDFT calculations to experimental precatalyst spectra, they can be further utilized to understand the equilibria discussed in Section 2.4 (see Supporting Information Section S8.1). The calculations corroborate that precatalysts can exist in complex equilibria featuring four-coordinate **Ni^{II}(IB)X_2**, five-coordinate **Ni^{II}(IB)(solv.)X_2**, or trimeric **[Ni^{II}(IB)X_2]$_3$ μ-X** species. Consistent with experiment, the calculated spectra for five-coordinate species and trimeric species exhibit a significant blue shift for the most intense calculated ligand field band (band 7; Figures S130–S132).

3.2 *Ab initio* Multireference Calculations of the Ni^{II}(IB)Cl_2 and Ni^{II}(IB)Br_2 Precatalysts

Due to the inherent complications with TDDFT described above, we have also used *ab initio* multireference calculations to compute and assign the experimentally observed ligand field excitations. First, we have systematically probed the effects of active space variation in CASSCF calculations (see Computational Details in Section S8 of the Supporting Information) on the qualitative agreement of **Ni^{II}(IB)Cl_2** and **Ni^{II}(IB)Br_2** with experimental spectra. Regardless of active space size (Tables S24–S39), the ground state is exclusively high spin. Notably, the largest active space used in this work, 22e,12o (five Ni 3*d* orbitals, six halide 2*p*/3*p* orbitals, and the Ni(IB) σ bonding orbital), results in a single-reference ground-state solution, with the highest weight of a single configuration in the CI vector of ~95% for both **Ni^{II}(IB)Cl_2** and **Ni^{II}(IB)Br_2** (Tables S29 and S35). This configuration corresponds to an $S = 1$ triplet ground state with unpaired electrons in the $d(x^2\text{-}y^2)$ and $d(xz)$ orbitals (i.e., the same configuration as obtained from DFT calculations; *cf.* Figure 7). We note that inclusion of the occupied halide 2*p*/3*p* orbitals and the Ni(IB) σ bonding orbital in the active space was essential to reproduce the experimental spectra. With this optimized active space, UV-vis-NIR absorption, CD, and MCD spectra of **Ni^{II}(IB)Cl_2** and **Ni^{II}(IB)Br_2** were calculated (Figure 8 and S141–S142). These calculations generally support assignments of experimental data given in Section 2.1 (Table 4). Individual states can be assigned based on the configuration state function with the largest weight in the CI vector, in conjunction with the location of the 3*d* holes (see Supporting Information Section S8.2).

Calculated signs for CD and MCD transitions are also consistent with experiment. All $^3A_2$ excited states exhibit experimental and calculated positive CD bands and negative MCD bands. The $^3A_1$ excited state (band 3 in experiment) exhibits negative bands for both CD and MCD. As supported by theory, the $^3B_1$ excited state exhibits a negative CD band and a positive MCD band. In contrast, the predicted sign for CD does not match that observed experimentally for the higher-energy $^3B_2$ excited state, though this is likely due to this transition being formally forbidden and gaining intensity through either spin-orbit or vibronic coupling, which can give either positive or negative differential intensity in CD.[46] The overall success of the CASSCF/CASPT2 approach in calculating UV-vis-NIR, and in

particular CD/MCD spectra, is especially encouraging for future analyses of experimental spectra for other chiral first row transition metal cross-coupling catalysts.

3.3 Computed Electrochemical Properties

Since the CASSCF CI vector indicates that the ground-state solutions are single-referent, we can use DFT to interpret the effects of different halide ligands on the $Ni^{III/II}$, $Ni^{II/I}$, and $Ni^{I/0}$ reduction potentials of the **Ni^{II}(IB)X_2** complexes and connect them to thermodynamically accessible redox pathways of Ni-based reductive cross-coupling catalysis. Table 5 provides computed potentials for various electrochemical processes (*vide supra*, Section 2.5). Experimentally, the reduction of **Ni^{II}(IB)X_2** complexes is chemically irreversible due to halide dissociation. DFT calculations predict slightly positive halide dissociation energies of ΔG_{dissoc}(CPCM) of ~6 kcal mol^{-1} and ~7 kcal mol^{-1} for Cl and Br **Ni^{I}(IB)X_2** complexes, respectively. The positive ΔG_{dissoc} may be associated with inaccuracies in halide solvation energy when using a simple CPCM. The high electrolyte concentration in electrochemical experiments, which is not accounted for in the computations, may also further shift the equilibrium toward dissociation. For comparison, the calculated ΔG_{dissoc} of halide loss from **Ni^{II}(IB)X_2** is significantly higher in energy (ΔG_{dissoc}(CPCM) = ~30 kcal mol^{-1} and ~29 kcal mol^{-1} for Cl and Br, respectively), indicating much stronger ligand–metal bonds for the Ni^{II} species.

The computed one-electron reduction potentials coupled to halide loss are −1.49 V and −1.39 V vs. $Fc^{+/0}$ for **Ni^{II}(IB)Cl_2** and **Ni^{II}(IB)Br_2**, respectively, with no additional coordinated solvent ligand (Table 5). The absolute calculated values compare well with those measured experimentally (Table 3), as does the calculated potential difference between the two complexes (Δ = ~0.10 V (~805 cm^{-1}) (calculated) vs. Δ = ~0.24 V (~1960 cm^{-1}) (experiment – average for all three solvents)). Thus, DFT calculations support the idea that stronger ligand fields generally lead to a more negative potential for Ni^{I} formation. In that regard, more facile reduction of **Ni^{II}(IB)Br_2** is attributed to the lower energy of the β-LUMOs by ~0.2 eV (Figure 7).

The computed one-electron reduction potentials coupled to halide loss also shift negatively upon solvent coordination. For the Cl complex, calculated values are −1.49 V, −1.65 V, and −1.66 V vs. $Fc^{+/0}$ for no solvent, MeCN, and DMA coordination, respectively. For the Br complex, analogous calculated values are −1.39 V, −1.48 V, and −1.44 V vs. $Fc^{+/0}$. These negative potential shifts due to solvent coordination are also ascribed to modifications of the Ni^{II} β-LUMOs. For example, average energy destabilizations of 0.40 eV and 0.47 eV are observed for **Ni^{II}(IB)Cl_2** and **Ni^{II}(IB)Br_2** complexes, respectively, upon MeCN or DMA coordination. Together, these calculations and the ligand field spectroscopy both indicate for the first time that the RAMO energy is an excellent descriptor of the redox properties of these metal-based cross-coupling catalysts, and DFT calculations provide a useful approach for analyzing ligand contributions to potentials.

Finally, further extending these calculations to additional species, the computed reduction of **Ni^{I}(IB)X** to **Ni^{0}(IB)X** or **Ni^{0}(IB)** is calculated to occur at exceedingly negative formal potentials (~−3 V to −4 V). These calculated potentials for Ni^{0} formation are significantly more negative than the reduction potentials of typical reductants used in cross-coupling

reactions (e.g., ~−1.11 V vs. $Fc^{+/0}$ in DMA for tetrakis(dimethylamino)ethylene (TDAE) or ~−1.94 V vs $Fc^{+/0}$ in DMF for Mn^0).[47,48] Similarly, the disproportionation of **Ni^{I}(IB)X** to **Ni^{II}(IB)X_2** and **Ni^0(IB)** is thermodynamically highly unfavorable, with a ΔG(CPCM) of ~+57 kcal mol^{-1} for both X = Cl and Br. Thus, Ni^0 is unlikely to be a catalytically relevant redox state. Bis(1,5-cyclooctadiene)nickel^0 (**Ni(COD)$_2$**), when used as the nickel source, likely first generates **Ni^{II}(IB)X_2** to commence the catalytic cycle. It is possible that **Ni^0(IB)** can be formed by mixing **IB** and **Ni(COD)$_2$**, and that this Ni^0 complex might oxidatively add one of the electrophiles to give **Ni^{II}(IB)RX** and initiate the first turnover. However, it is unlikely that the catalytic cycle involves reduction back to **Ni^0(IB)**.

3.4 Resting State Electronic Structure and its Contributions to Reactivity

The electronic structure and electrochemical properties determined herein for **Ni^{II}(IB)X_2** complexes support a $Ni^{I/III}$ cross-coupling reaction cycle. A low-spin square planar Ni^{II} phenanthroline (phen) aryl halide (**Ni^{II}(phen)(Ar)X**) resting state has been proposed by Diao *et al.* for Ni-catalyzed reductive 1,2–dicarbofunctionalization of alkenes.[49] This resting state is thought to form from **Ni^{I}(phen)X** bimolecular oxidative addition of the aryl halide. The **Ni^{II}(phen)(Ar)X** is anticipated to react rapidly with C(sp^3) radicals to produce a five-coordinate **Ni^{III}(phen)(Ar)X** intermediate.[31] The 'R−Ar' cross-coupled product can then form via reductive elimination. The analogous reactivity considerations for **IB** complexes and vinyl halides are given in Figure 9.[44]

Given the ability to accurately calculate and reproduce experimental formal potentials, the same approach can be used to investigate the bonding and redox properties of the **Ni^{II}(IB)(Vn)Br** (Vn = 1-methyl-4-vinylbenzene; Figure 9) resting state, which we were unable to isolate and study electrochemically due to instability.[44] The calculated reduction potential of this species coupled to halide loss is −1.82 V vs. $Fc^{+/0}$ in DMA. Interestingly, this is ~0.4 V more negative than that calculated for reduction of **Ni^{II}(IB)Br_2**. The less facile reduction of **Ni^{II}(IB)(Vn)Br** relative to **Ni^{II}(IB)Br_2** likely stems from the increased donor strength of the Vn co-ligand (relative to Br). In the low-spin state of **Ni^{II}(IB)(Vn)Br**, the Ni^{II} $d(x^2\text{-}y^2)$ orbital is the RAMO for the $Ni^{II/I}$ couple. Strong antibonding interactions within the RAMO will destabilize the energy of this orbital, which will decrease the electron affinity and, thus, result in a more negative reduction potential. In this respect, it is also noted that, across a series of various para-substituted styrenyl derivatives, the calculated $Ni^{II/I}$ reduction potentials of the **Ni^{II}(IB)(Vn)Br** species (coupled to halide dissociation) trend with the Hammett parameters of the substituent and the Ni^{II} character in the $d(x^2\text{-}y^2)$ RAMO obtained from Löwdin population analysis (Figure S90).

It is also instructive to consider the role of the Vn ligand in the benzyl-C(sp^3) radical recombination with **Ni^{II}(IB)(Vn)X**. The high donation of the Vn co-ligand in **Ni^{II}(IB)(Vn)X** would make this intermediate more oxidizable and readily available for the less-exergonic radical coupling; this variation in donation should also be correlated to changes in Ni^{II}–ligand bond covalency. Indeed, the calculated ligand–metal covalency of **Ni^{II}(IB)(Vn)Br** varies linearly with the calculated energy of the RAMO (Figure 10A). **Ni^{II}(IB)(Vn)Br** styrenyl systems with either dimethylamino or carbomethoxy substituents at the four position feature ~62% 3*d* character vs. ~10% 3*d* character in the RAMO, which correlate

to more negative and less negative RAMO energies, respectively. Previous studies have also observed a linear correlation between redox potential and covalency in metalloproteins and model complexes.[50–53]

The less-donating halide ligands (relative to the Vn ligand) could electronically disfavor trapping of **Ni^{II}(IB)X$_2$** with benzylic radicals; this interpretation is supported by DFT calculations with **Ni$^{II/III}$(IB)X$_2$** oxidation potentials that are >1 V negative of oxidation potentials of **Ni$^{II/III}$(IB)(Vn)Br** (Figure 10B). The electronic influence of the Vn co-ligand can thus be envisioned as enhancing the kinetically competent radical recombination relative to deleterious side reactivity of the free benzylic radical. Indeed, there is a reasonable match between the calculated oxidation energies of the benzylic radicals and **Ni^{II}(IB)(Vn)Br** species, leading to favorable (near-ergoneutral) radical recombination reactions (Table S9). Additionally, there is a direct correlation between calculated oxidation potential gaps (ΔE_{ox} between the benzyl-C(sp^3) radical and **Ni^{II}(IB)(Vn)Br** species) and reaction yields obtained from coupling the benzylic radicals generated from the NHP esters (NHP = *N*-hydroxyphthalimide),[54] with the highest yields observed for reactions between benzyl-C(sp^3) radicals and **Ni^{II}(IB)(Vn)Br** species with calculated oxidation potential gaps (ΔE_{ox}) of ~−0.4 V (Figure 10C). Although care must be taken drawing mechanistic conclusions from reaction yields, given that 1) **Ni^{II}(IB)(Vn)X** is the catalyst resting state[44] (*vide infra*), and 2) Ni is not involved in generating the radical from the NHP ester, the correlation between reaction yield and ΔE_{ox} reflects the favorability of the radical addition to **Ni^{II}(IB)(Vn)Br**.

4. Discussion

Due to their disparate electronic structures relative to precious metal analogs, first-row transition metal catalysts unlock a rich area of exploration for the discovery of new organic reactions. Indeed, many novel bond constructions have been discovered recently.[2] Exciting mechanistic studies have also highlighted a variety of inorganic species of relevance to reactivity, many of which feature interesting metal- and ligand-based redox events. Furthermore, ground state cross-coupling reaction mechanisms of first-row transition metal complexes have direct relevance to the thermal components of photoredox catalysis. Unlike their bipyridine and terpyridine analogues, which feature intense MLCT transitions, non-conjugated ligands (e.g., **IB**) exhibit rich ligand field spectral features that can be utilized to interrogate Ni-based electronic structure, and just as transient spectroscopic methods can provide insights into the light-induced components of photoredox mechanisms,[55] steady state spectroscopic methods can also provide direct insights into electronic structure contributions to transition metal reactivity.[12,56,57]

Here we have provided several new insights into the area of cross-coupling catalysis: 1) a combination of electronic and magneto-optical spectroscopic methods has allowed for a detailed analysis and definition of the ligand field excited state manifolds of two previously employed cross-coupling catalysts, **Ni^{II}(IB)Cl$_2$** and **Ni^{II}(IB)Br$_2$**. This analysis has allowed for the quantification of relative ligand field strengths. As discussed further below, we demonstrate how ligand field strength is linked directly to changes in the energy of the Ni-based RAMO and, thus, to reduction potentials. 2) VT UV-vis-NIR spectroscopy has

uncovered and identified two equilibrium processes that we believe to be significant for cross-coupling reaction mechanisms and yields. These equilibria feature a) four-coordinate and five-coordinate Ni^{II} complexes when in DMA, and b) a monomeric and trimeric species in the Cl complex when in DCM. 3) The Vn ligand involved in cross-coupling plays a critical role in directing the reactivity of the putative resting Ni^{II} complex. Specifically, the electronic nature of the Vn ligand tunes the Ni-based covalency over a large range. In doing so, the covalent character modulates the reactivity of this species toward C(sp^3) radicals, and we have observed a direct correlation between previously reported reaction yields[58] and the difference in oxidation potential between the Ni^{II} resting state and the C(sp^3) radicals, which reflects the driving force for the radical recombination reaction between these species.

Averaging all assignable, spin-allowed ligand field excited states, it was demonstrated in Section 2.1 that the ligand field strength of the Cl complex is ~390 cm^{-1} stronger than the Br complex. In Section 2.5, it was shown that one-electron reduction of **Ni^{II}(IB)X_2** complexes is coupled to rapid halide dissociation, and it is on average (over three solvents) ~0.24 V (~1960 cm^{-1}) harder to reduce the Cl complex relative to the Br complex. In Section 3.3, it was also demonstrated that electronic structure calculations can accurately reproduce the experimental one-electron reduction potentials and that the origin of the relative reduction potential arises from ligand field (de)stabilization of the Ni^{II}-based RAMO. Thus, combining ligand field spectroscopies with electrochemistry and electronic structure calculations provides a direct means to dissect geometric and electronic structure contributions to catalytically-relevant redox potentials and allows for an experimentally calibrated approach to extend computations to reaction intermediates.

While the ligand perturbations studied here are halide-based, the ligand field spectral features of Ni-catalysts will also be highly sensitive to ligand perturbations. For example, in Table 6, we have compiled electronic transitions for the **IB** complexes and a series of previously reported pseudo-T_d Ni^{II} complexes, with structures shown in Figure 11.[59–63] In general, the second $^3B_1 \rightarrow {}^3A_2(F)$ transition, which is the most intense observed in the lower-energy ligand field manifold, tracks roughly with the overall ligand field strength, with $Ni^{II}(PPh_3)_2Cl_2$ exhibiting the highest transition energy. Another noticeable trend, the variability in $^3B_1/^3B_2$ transition energies, stems from high variability in geometric distortions. We also note the similarity in blueshifts in transition energies for **Ni^{II}(IB)X_2** and $Ni^{II}(L+)X_3$ as a function of halide identity. Thus, measured ligand field transitions can provide a means to estimate specific ligand contributions to catalyst electronic structure and ultimately redox potentials and reactivity in future studies.

VT electronic absorption spectra reported here are also particularly illuminating and provide 1) direct evidence of variable speciation for **IB** complexes as a function of solvent and temperature and 2) direct thermodynamic parameters describing these equilibria. For **Ni^{II}(IB)Cl_2** and **Ni^{II}(IB)Br_2** in DMA, a significant fraction of DMA coordinated complex is present at room temperature (~37% and 49%, respectively, at 3.6 mM (Cl) and 3.5 mM (Br)). At lower temperatures (273 K), DMA coordination is strongly favored (~53% and 69%, respectively). Generally, amide-based solvents can coordinate to metal centers through the carbonyl oxygen, preference for which is further influenced by steric hindrance at the nitrogen center. The $n_N \rightarrow \pi^*_{CO}$ delocalization of the amide results in increased

electron density on oxygen (Figure 5), leading to a strong donor and a partial negative charge near the Ni^{II} center.[69] As demonstrated herein for the first time by a combination of electrochemistry and electronic structure calculations, DMA coordination can lead to a more difficult to reduce Ni^{II} center, with negatively shifted potentials of ~200 mV in DMA vs. MeCN for the Cl and Br complexes. The single electron reduction leads to rupture of the halide–metal bond; we propose that halide solvation and solvent coordination to Ni can also contribute significantly to the measured reduction potential (e.g., –1.47 V vs. $Fc^{+/0}$ in DMA/DCM for **Ni^{II}(IB)Cl_2**). Of further note, yields for reductive alkenylation are maximized when 1) DMA or another amide solvent is utilized, and 2) the reaction temperature is lowered to 0–5 °C, with both considerations favoring nickel coordination by the solvent.

Scheme 2 provides boron trifluoride (BF_3) donor numbers, acceptor numbers, substrate conversion percentage, and cross-coupled yield percentages for the reaction between (1-chloroethyl)benzene and (*E*)-1-(2-bromovinyl)-4-methoxybenzene. Previous studies determined the optimized conditions based on systematic screening of reaction parameters.[7] We conducted triplicate measurements of this reaction in several solvents with a range of Lewis basicities. Generally, as the donicity of the solvent decreases, the substrate consumption and cross-coupled product yield decrease significantly. As discussed further below, we believe this reflects a significant steric effect at play, which can protect Ni^{II} and/or reduced Ni^{I} species from off-cycle reactivity. Based on these considerations, we also purport that amide coordination results in a more oxidizable Ni^{I} species, which increases oxidative addition reactivity.

The VT UV-vis-NIR and spectroelectrochemistry studies, when compared with experimental conditions often utilized for nickel-catalyzed reductive cross-coupling (i.e., low temperatures, use of coordinating solvents, relatively mild reducing agents, etc.),[2,7,8] are consistent with the mechanistic investigation of this reaction by Turro and coworkers,[44] which suggests this reaction proceeds via a $Ni^{I/III}$ redox cycle (Scheme 3), similar to that proposed by Diao and coworkers for the related cross-coupling of aryl halides.[20] Additional aspects of the optimized reaction conditions can be commented on, however, as derived from the findings in the present study.

To better understand their role in the cross-coupling of (*E*)-1-(2-bromovinyl)-4-methylbenzene (Vn $C(sp^2)$ component) and (1-bromoethyl)benzene ($C(sp^3)$ radical), DFT computed stable intermediates along the nickel catalytic cycle are shown in Scheme 3 for **Ni^{II}(IB)Br_2**. Free energies of individual steps are energetically accessible, suggesting favorable cross-coupling reactivity. Note that the C–C bond forming cycle is identical regardless of the $C(sp^3)$ benzyl radical source. However, two distinct pathways to generating these radicals have been proposed by Turro *et al.*, which differ in terms of substrate (i.e., benzyl halide, pathway A, or NHP ester, pathway B) and reductant (i.e., Mn^0 vs. TDAE reductants) (Scheme 3).[44] We also note Scheme 3 only features computed free energies, and we have restricted our discussion of the possible effects of DMA to these steps/energies. It is also possible for DMA coordination to influence reaction barriers. More detailed mechanistic aspects and reaction kinetics are discussed in reference 44 by Turro *et al.*. More

broadly, results described herein suggest future computational studies should also consider explicit solvent coordination in calculated reaction mechanisms.

With benzyl bromide and a Mn^0 reductant, the only computed endergonic reaction in the catalytic cycle is the radical recombination of the C(sp^3) radical with **Ni^{II}(IB)(Vn)Br** to form **Ni^{III}(IB)(Vn)(R)Br** (Scheme 3, reaction 3, ΔG^0(CPCM) = 4.6 kcal/mol). Notably, **Ni^{II}(IB)(Vn)Br** and related species have been assigned as the catalytic resting state.[49,20,44] The generation of C(sp^3) benzyl radical from benzyl bromide is a favorable process through Br-atom abstraction (reaction ii.A) with either **Ni^{I}(IB)Vn** (ΔG^0(CPCM) = −19.1 kcal mol^{-1}) or **Ni^{I}(IB)Br** (−9.3 kcal mol^{-1}), thus suggesting there might be a balance between this reactivity pathway and reactions *i.A* and *ii.A* in Scheme 3. The detailed kinetic analysis presented in ref. [44], however, suggests that XAT from Ni^{II}(IB)X is a more likely alternative, as also evidenced by the observed reactivity of Ni^{I}(IB)X with both C(sp^2) vinyl- and C(sp^3) benzyl-halides.

With the NHP ester substrate and TDAE as a reductant, the **Ni^{I}(IB)Br** formation from **Ni^{II}(IB)Br_2** becomes slightly disfavored with ΔG^0(CPCM) = 1.1 kcal/mol, in addition to the only endergonic reaction 3 in pathway A. In this scenario, the C(sp^3) benzyl radical can be generated from NHP ester without Ni involvement through a direct reduction with TDAE (reaction *i.B*, $E_{1/2}$ = −1.39 V vs. $Fc^{+/0}$)) followed by a highly exergonic decomposition, yielding CO_2, phthalimide anion, and C(sp^3) benzyl radical (pathway *i.B*).

As discussed, higher yields of cross-coupled product are typically obtained at lower temperatures and in coordinating solvents, supporting solvent coordination as a key component for the catalytic cycle.[2,7,8] The computed free energies indeed suggest an equilibrium might exist between the **Ni^{I}(IB)Br** and the **[Ni^{I}(IB)Br]$_2$ μ-Br** dimeric species (ΔG^0(CPCM) = +4.1 kcal/mol). We speculate low temperature, which entropically favors solvent coordination, might prevent highly reactive Ni^{I} intermediates from entering off-cycle pathways, especially toward forming oligomeric (e.g., dimeric/trimeric) species. The same could be true for Ni^{II} species. Coordinating solvents can similarly protect Ni^{I} from dimerization by forming a more favorable equilibrium between **Ni^{I}(IB)Br ↔ Ni^{I}(IB)(S)Br**, where S = solvent, since formation of the dimer from **Ni^{I}(IB)(S)Br** intermediate may be disfavored sterically. Although the ΔG^0 for DMA coordination to **Ni^{I}(IB)Br** is computed to be higher than ΔG^0 for dimerization (~6.9 kcal mol^{-1} vs. ~4.1 kcal mol^{-1}), the large excess of DMA (especially relative to the rather low concentration of **Ni^{I}(IB)Br** under catalytic conditions) will favor solvent coordination and further perturb the relative concentrations/equilibria for both processes.

DMA coordination to **Ni^{I}(IB)X** could also lower the kinetic barrier for bimolecular oxidative addition reactivity in reaction 2 (Scheme 3): 1) the **Ni^{I}(IB)X** oxidation to **Ni^{II}(IB)X_2** is favored in DMA, as observed by the negative shift in reduction potential in the experimental cyclic voltammetry, and 2) oxidative addition of vinyl-halide to **Ni^{I}(IB)X** forming **Ni^{II}(IB)(Vn)X** is favored due to increased electron density on the Ni center and destabilized frontier molecular orbitals upon DMA coordination.

In addition to insights into the role of solvent coordination, the Vn ligand itself can strongly contribute to the reactivity of the resting state. Indeed, there is a linear trend between the amount of metal character in the RAMO and its energy (Figure 10A). In general, ligand contributions to the destabilization of the energy of the RAMO will result in greater reactivity and easier oxidation. Notably, we observed a correlation between the reaction yields and the difference in oxidation potentials of **Ni^{II}(IB)(Vn)Br** and benzyl-C(sp^3) radical (ΔE_{ox}). The same metric was recently proposed by Okamoto *et al.* as a measure of the probability of intramolecular redox reactions, showing the most favorable radical recombination for ΔE_{ox} ~0 V.[71] In our case, the coupling efficiency and resulting yields maximize when the benzyl-C(sp^3) radical oxidation potential is slightly higher (by ~0.4 V) than the oxidation potential of **Ni^{II}(IB)(Vn)Br**. A higher reactivity of the benzyl-C(sp^3) radical might be necessary to overcome the reorganization energy required for the change in coordination geometry of the Ni catalyst upon formation of a five-coordinate **Ni^{III}(IB)(R)(Vn)Br** intermediate. Lower yields at higher oxidation potentials of the benzyl-C(sp^3) radicals could be similarly justified by accessing side-reaction radical pathways (e.g., homocoupling). The calculated mismatch in the oxidation potentials may also be a computational artifact. Although we have demonstrated a reasonable correlation between computed and experimental electrochemical data, the nature of Ni catalysts and small organic radicals is quite different and could result in varied relative accuracy of the computed oxidation potentials. The computational model also neglects explicit solvation, whereas DMA solvation and/or coordination to the Ni catalyst (as demonstrated in the present study) could shift the observed oxidation potentials. Regardless, there is a clear trend between the calculated ΔE_{ox} and reaction yields, which indicates the relative oxidation potentials and frontier molecular orbitals of the **Ni^{II}(IB)(Vn)Br** resting state and the benzyl-C(sp^3) radicals may be a useful predictor for reactivity and can be utilized to computationally screen and guide the synthesis of new Ni complexes for reductive cross-coupling catalysis.

Conclusions

We have presented the first comprehensive spectroscopic, electrochemical, and computational study of Ni^{II}-based chiral reductive cross-coupling catalysts, **Ni^{II}(IB)Cl$_2$** and **Ni^{II}(IB)Br$_2$**. This combination of methods has established 1) there is a direct connection between ligand field strength and catalytically relevant Ni-based reduction potentials, 2) there exists variable speciation for **IB** complexes as a function of solvent and temperature, and VT spectroscopy provides a means to directly measure thermodynamic parameters describing these equilibria, and 3) the Vn ligand involved in cross-coupling plays a critical role in directing the reactivity of the putative resting Ni^{II} complex through strong modulation of ligand–metal covalency. These experimental findings strongly support a critical steric and electronic role that amide-based solvents play in the cross-coupling catalytic cycle. Through this electronic structural characterization, we suggest that dimerization or oligomerization of the catalyst is inhibited by solvent coordination. Furthermore, the modification of electronic structure through solvent coordination increases the driving force for oxidative addition, as evidenced by formal potentials from voltammetry. These results highlight the importance of reaction conditions on catalytic efficiencies and will guide future methodology studies,

as well as the development of new ligand scaffolds for Ni-based reductive cross-coupling catalysis.

Supplementary Material

Refer to Web version on PubMed Central for supplementary material.

Acknowledgment

We acknowledge the X-ray Crystallography Facility in the Beckman Institute at Caltech, and the Dow Next Generation Instrumentation Grant for X-ray structure collection. Some computations presented here were conducted in the Resnick High Performance Computing Center, a facility supported by Resnick Sustainability Institute at the California Institute of Technology. We are grateful for assistance from Alexander Q. Cusumano in collecting vibrational circular dichroism data and from Michael Zott in collecting variable temperature UV-vis-NIR spectra. We thank Harry B. Gray and Jay R. Winkler for helpful discussions on equilibrium processes in spectroscopy and David E. Hill and David A. Cagan for helpful general discussions. N.P.K. acknowledges support from the Hertz Fellowship and from the National Science Foundation Graduate Research Fellowship under Grant No. DGE-1745301. This project has received funding from the European Union's Horizon 2020 research and innovation programme under the Marie Sklodowska-Curie grant agreement No. 883987 (D.B.). Support has been provided by the Grant Agency of the Czech Republic (20–06451Y to J.C.). Support has been provided by the National Institutes of Health (National Institute of General Medical Sciences, R35-GM142595) (R.G.H.). S.E.R. acknowledges financial support from the NIH (R35GM118191).

References

(1). Semmelhack MF; Helquist PM; Jones LD Synthesis with Zerovalent Nickel. Coupling of Aryl Halides with Bis(1,5-Cyclooctadiene)Nickel(0). J. Am. Chem. Soc. 1971, 93 (22), 5908–5910. 10.1021/ja00751a062.

(2). Poremba KE; Dibrell SE; Reisman SE Nickel-Catalyzed Enantioselective Reductive Cross-Coupling Reactions. ACS Catal. 2020, 10 (15), 8237–8246. 10.1021/acscatal.0c01842. [PubMed: 32905517]

(3). Durandetti M; Nédélec J-Y; Périchon J Nickel-Catalyzed Direct Electrochemical Cross-Coupling between Aryl Halides and Activated Alkyl Halides. J. Org. Chem. 1996, 61 (5), 1748–1755. 10.1021/jo9518314. [PubMed: 11667045]

(4). Durandetti M; Gosmini C; Périchon J Ni-Catalyzed Activation of α-Chloroesters: A Simple Method for the Synthesis of α-Arylesters and β-Hydroxyesters. Tetrahedron 2007, 63 (5), 1146–1153. 10.1016/j.tet.2006.11.055.

(5). Cherney AH; Kadunce NT; Reisman SE Catalytic Asymmetric Reductive Acyl Cross-Coupling: Synthesis of Enantioenriched Acyclic α,α-Disubstituted Ketones. J. Am. Chem. Soc. 2013, 135 (20), 7442–7445. 10.1021/ja402922w. [PubMed: 23634932]

(6). Hofstra JL; Cherney AH; Ordner CM; Reisman SE Synthesis of Enantioenriched Allylic Silanes via Nickel-Catalyzed Reductive Cross-Coupling. J. Am. Chem. Soc. 2018, 140 (1), 139–142. 10.1021/jacs.7b11707. [PubMed: 29202243]

(7). Cherney AH; Reisman SE Nickel-Catalyzed Asymmetric Reductive Cross-Coupling Between Vinyl and Benzyl Electrophiles. J. Am. Chem. Soc. 2014, 136 (41), 14365–14368. 10.1021/ja508067c. [PubMed: 25245492]

(8). DeLano TJ; Reisman SE Enantioselective Electroreductive Coupling of Alkenyl and Benzyl Halides via Nickel Catalysis. ACS Catal. 2019, 9 (8), 6751–6754. 10.1021/acscatal.9b01785. [PubMed: 32351776]

(9). Cagan DA; Bím D; Silva B; Kazmierczak NP; McNicholas BJ; Hadt RG Elucidating the Mechanism of Excited-State Bond Homolysis in Nickel–Bipyridine Photoredox Catalysts. J. Am. Chem. Soc. 2022, 144 (14), 6516–6531. 10.1021/jacs.2c01356. [PubMed: 35353530]

(10). Cagan DA; Bîm D; McNicholas BJ; Kazmierczak NP; Oyala PH; Hadt RG Photogenerated Ni(I)–Bipyridine Halide Complexes: Structure-Function Relationships for Competitive C(sp2)–Cl Oxidative Addition and Dimerization Reactivity Pathways. Inorg. Chem. 2023, 62, 9538–9551. [PubMed: 37279403]

(11). Gao Y; Hill DE; Hao W; McNicholas BJ; Vantourout JC; Hadt RG; Reisman SE; Blackmond DG; Baran PS Electrochemical Nozaki–Hiyama–Kishi Coupling: Scope, Applications, and Mechanism. J. Am. Chem. Soc. 2021, 143 (25), 9478–9488. 10.1021/jacs.1c03007. [PubMed: 34128671]

(12). Daifuku SL; Al-Afyouni MH; Snyder BER; Kneebone JL; Neidig ML A Combined Mössbauer, Magnetic Circular Dichroism, and Density Functional Theory Approach for Iron Cross-Coupling Catalysis: Electronic Structure, In Situ Formation, and Reactivity of Iron-Mesityl-Bisphosphines. J. Am. Chem. Soc. 2014, 136 (25), 9132–9143. 10.1021/ja503596m. [PubMed: 24918160]

(13). Day CS; Somerville RJ; Martin R Deciphering the Dichotomy Exerted by Zn(Ii) in the Catalytic sp2 C–O Bond Functionalization of Aryl Esters at the Molecular Level. Nature Catalysis 2021, 4 (2), 124–133. 10.1038/s41929-020-00560-3.

(14). Jensen AE; Knochel P Nickel-Catalyzed Cross-Coupling between Functionalized Primary or Secondary Alkylzinc Halides and Primary Alkyl Halides. J. Org. Chem. 2002, 67 (1), 79–85. 10.1021/jo0105787. [PubMed: 11777442]

(15). Dorval C; Gosmini C Low-Valent Cobalt Complexes in C–X Coupling and Related Reactions. In Cobalt Catalysis in Organic Synthesis; 2020; pp 163–205. 10.1002/9783527814855.ch5.

(16). Cahiez G; Marquais S Highly Chemo- and Stereoselective Fe-Catalyzed Alkenylation of Organomanganese Reagents. Tetrahedron Letters 1996, 37 (11), 1773–1776. 10.1016/0040-4039(96)00116-5.

(17). Cahiez G; Marquais S Copper-Catalyzed Alkylation of Organomanganese Chloride Reagents. Synlett 2002, 1993 (01), 45–47.

(18). Cahiez G; Avedissian H Cobalt-Catalyzed Alkenylation of Organomagnesium Reagents. Tetrahedron Letters 1998, 39 (34), 6159–6162. 10.1016/S0040-4039(98)01266-0.

(19). Yanagi T; Somerville RJ; Nogi K; Martin R; Yorimitsu H Ni-Catalyzed Carboxylation of C(Sp2)–S Bonds with CO2: Evidence for the Multifaceted Role of Zn. ACS Catal. 2020, 10 (3), 2117–2123. 10.1021/acscatal.9b05141.

(20). Ju L; Lin Q; LiBretto NJ; Wagner CL; Hu CT; Miller JT; Diao T Reactivity of (Bi-Oxazoline)Organonickel Complexes and Revision of a Catalytic Mechanism. J. Am. Chem. Soc. 2021, 143 (36), 14458–14463. 10.1021/jacs.1c07139. [PubMed: 34463481]

(21). Xu J; Li Z; Xu Y; Shu X; Huo H Stereodivergent Synthesis of Both Z- and E-Alkenes by Photoinduced, Ni-Catalyzed Enantioselective C(sp3)–H Alkenylation. ACS Catal. 2021, 11 (21), 13567–13574. 10.1021/acscatal.1c04314.

(22). Lu Q; Guan H; Wang Y-E; Xiong D; Lin T; Xue F; Mao J Nickel/Photoredox-Catalyzed Enantioselective Reductive Cross-Coupling between Vinyl Bromides and Benzyl Chlorides. J. Org. Chem. 2022, 87 (12), 8048–8058. 10.1021/acs.joc.2c00707. [PubMed: 35666844]

(23). Liu J; Gong H; Zhu S Nickel-Catalyzed, Regio- and Enantioselective Benzylic Alkenylation of Olefins with Alkenyl Bromide. Angewandte Chemie International Edition 2021, 60 (8), 4060–4064. 10.1002/anie.202012614. [PubMed: 33171012]

(24). Zhu Z; Lin L; Xiao J; Shi Z Nickel-Catalyzed Stereo- and Enantioselective Cross-Coupling of Gem-Difluoroalkenes with Carbon Electrophiles by C−F Bond Activation. Angewandte Chemie International Edition 2022, 61 (6), e202113209. 10.1002/anie.202113209. [PubMed: 34889493]

(25). Hu X; Cheng-Sánchez I; Cuesta-Galisteo S; Nevado C Nickel-Catalyzed Enantioselective Electrochemical Reductive Cross-Coupling of Aryl Aziridines with Alkenyl Bromides. J. Am. Chem. Soc. 2023. 10.1021/jacs.2c12869.

(26). Jiang Y; Yang K; Wei Y; Wang Q; Li S-J; Lan Y; Koh MJ Catalytic Multicomponent Synthesis of C-Acyl Glycosides by Consecutive Cross-Electrophile Couplings. Angewandte Chemie International Edition 2022, 61 (46), e202211043. 10.1002/anie.202211043. [PubMed: 36165541]

(27). Geng J; Sun D; Song Y; Tong W; Wu F Ni-Catalyzed Asymmetric Reductive Alkenylation of α-Chlorosulfones with Vinyl Bromides. Org. Lett. 2022, 24 (9), 1807–1811. 10.1021/acs.orglett.2c00217. [PubMed: 35234038]

(28). Duan M; Wang Y; Zhu S Nickel-Catalyzed Asymmetric 1,2-Alkynylboration of Vinylarenes. Tetrahedron Letters 2023, 114, 154247. 10.1016/j.tetlet.2022.154247.

(29). Sun D; Ma G; Zhao X; Lei C; Gong H Nickel-Catalyzed Asymmetric Reductive Arylation of α-Chlorosulfones with Aryl Halides. Chem. Sci. 2021, 12 (14), 5253–5258. 10.1039/D1SC00283J. [PubMed: 34168777]

(30). Ye Y; Liu J; Xu B; Jiang S; Bai R; Li S; Xie T; Ye X-Y Nickel-Catalyzed Enantioselective 1,2-Vinylboration of Styrenes. Chem. Sci. 2021, 12 (39), 13209–13215. 10.1039/D1SC04071E. [PubMed: 34745552]

(31). Lin Q; Spielvogel EH; Diao T Carbon-Centered Radical Capture at Nickel(II) Complexes: Spectroscopic Evidence, Rates, and Selectivity. Chem 2023, 9 (5), 1295–1308. 10.1016/j.chempr.2023.02.010.

(32). Laurence C; Gal JF Lewis Basicity and Affinity Scales: Data and Measurements; Wiley, New York, 2010.

(33). Classification of Solvents. In Solvents and Solvent Effects in Organic Chemistry; 2010; pp 65–106. 10.1002/9783527632220.ch3.

(34). Best SP; Clark RJH The Identification of an Electronic Raman Transition for the Hexa-Aquavanadium(III) Ion. A Direct Spectroscopic Determination of the Trigonal Field Splitting of the 3T1g Ground Term. Chemical Physics Letters 1985, 122 (4), 401–405. 10.1016/0009-2614(85)80245-1.

(35). Pescitelli G; Lüdeke S; Chamayou A-C; Marolt M; Justus V; Górecki M; Arrico L; Di Bari L; Islam MA; Gruber I; Enamullah M; Janiak C Broad-Range Spectral Analysis for Chiral Metal Coordination Compounds: (Chiro)Optical Superspectrum of Cobalt(II) Complexes. Inorg. Chem. 2018, 57 (21), 13397–13408. 10.1021/acs.inorgchem.8b01932.

(36). Lu R; Yang T; Chen X; Fan W; Chen P; Lin Z; Liu G Enantioselective Copper-Catalyzed Radical Cyanation of Propargylic C–H Bonds: Easy Access to Chiral Allenyl Nitriles. J. Am. Chem. Soc. 2021, 143 (36), 14451–14457. 10.1021/jacs.1c07190. [PubMed: 34477365]

(37). Hofstra JL Development and Mechanistic Studies of Ni-Catalyzed Asymmetric Reductive Cross-Coupling Reactions, California Institute of Technology, 2019. https://resolver.caltech.edu/CaltechTHESIS:06012019-034543690.

(38). Kazmierczak NP; Chew JA; Vander Griend DA Bootstrap Methods for Quantifying the Uncertainty of Binding Constants in the Hard Modeling of Spectrophotometric Titration Data. Analytica Chimica Acta 2022, 1227, 339834. 10.1016/j.aca.2022.339834. [PubMed: 36089297]

(39). Vander Griend DA; Bediako DK; DeVries MJ; DeJong NA; Heeringa LP Detailed Spectroscopic, Thermodynamic, and Kinetic Characterization of Nickel(II) Complexes with 2,2'-Bipyridine and 1,10-Phenanthroline Attained via Equilibrium-Restricted Factor Analysis. Inorg. Chem. 2008, 47 (2), 656–662. 10.1021/ic700553d. [PubMed: 18095670]

(40). Espinoza EM; Clark JA; Soliman J; Derr JB; Morales M; Vullev VI Practical Aspects of Cyclic Voltammetry: How to Estimate Reduction Potentials When Irreversibility Prevails. J. Electrochem. Soc. 2019, 166 (5), H3175–H3187. 10.1149/2.0241905jes.

(41). Tang T; Jones E; Wild T; Hazra A; Minteer SD; Sigman MS Investigating Oxidative Addition Mechanisms of Allylic Electrophiles with Low-Valent Ni/Co Catalysts Using Electroanalytical and Data Science Techniques. J. Am. Chem. Soc. 2022, 144 (43), 20056–20066. 10.1021/jacs.2c09120. [PubMed: 36265077]

(42). Bard AJ; Faulkner LR; White HS Electrochemical Methods: Fundamentals and Applications, 3rd ed.; John Wiley & Sons, Inc.: Hoboken, NJ, USA, 2022.

(43). Zhou Y-Y; Uyeda C Reductive Cyclopropanations Catalyzed by Dinuclear Nickel Complexes. Angewandte Chemie International Edition 2016, 55 (9), 3171–3175. 10.1002/anie.201511271. [PubMed: 26822193]

(44). Turro RF; Wahlman JLH; Tong ZJ; Chen X; Yang M; Chen EP; Hong X; Hadt RG; Yang Y-F; Houk KN; Reisman SE Mechanistic Investigation of Ni-Catalyzed Reductive Cross-Coupling of Alkenyl and Benzyl Electrophiles. J. Am. Chem. Soc. 2023, 145 (27), 14705–14715. 10.1021/jacs.3c02649. [PubMed: 37358565]

(45). Li G; Brady MD; Meyer GJ Visible Light Driven Bromide Oxidation and Ligand Substitution Photochemistry of a Ru Diimine Complex. J. Am. Chem. Soc. 2018, 140 (16), 5447–5456. 10.1021/jacs.8b00944. [PubMed: 29595247]

(46). Harding MJ; Mason SF; Robbins DJ; Thomson AJ Magnetic Circular Dichroism Spectra of Some Nickel(II) Complexes. Part I. The Temperature Dependence of the Spectrum of the Nickel(II) Hexaquo-Ion. J. Chem. Soc. A 1971, No. 0, 3047–3058. 10.1039/J19710003047.

(47). Burkholder C; Dolbier WR; Médebielle M Tetrakis(Dimethylamino)Ethylene as a Useful Reductant of Some Bromodifluoromethyl Heterocycles. Application to the Synthesis of New Gem-Difluorinated Heteroarylated Compounds. J. Org. Chem. 1998, 63 (16), 5385–5394. 10.1021/jo980201+.

(48). Gaur JN; Goswami NK Kinetics of the Reduction of Mn^{2+} at the Dropping Mercury Electrode in Non-Aqueous Media. Electrochimica Acta 1967, 12 (11), 1489–1493. 10.1016/0013-4686(67)80064-1.

(49). Lin Q; Diao T Mechanism of Ni-Catalyzed Reductive 1,2-Dicarbofunctionalization of Alkenes. J. Am. Chem. Soc. 2019, 141 (44), 17937–17948. 10.1021/jacs.9b10026. [PubMed: 31589820]

(50). Anxolabéhère-Mallart E; Glaser T; Frank P; Aliverti A; Zanetti G; Hedman B; Hodgson KO; Solomon EI Sulfur K-Edge X-Ray Absorption Spectroscopy of 2Fe–2S Ferredoxin: Covalency of the Oxidized and Reduced 2Fe Forms and Comparison to Model Complexes. J. Am. Chem. Soc. 2001, 123 (23), 5444–5452. 10.1021/ja010472t. [PubMed: 11389625]

(51). Dey A; Jenney FE; Adams MWW; Babini E; Takahashi Y; Fukuyama K; Hodgson KO; Hedman B; Solomon EI Solvent Tuning of Electrochemical Potentials in the Active Sites of HiPIP Versus Ferredoxin. Science 2007, 318 (5855), 1464–1468. 10.1126/science.1147753. [PubMed: 18048692]

(52). Dey A; Okamura T; Ueyama N; Hedman B; Hodgson KO; Solomon EI Sulfur K-Edge XAS and DFT Calculations on P450 Model Complexes: Effects of Hydrogen Bonding on Electronic Structure and Redox Potentials. J. Am. Chem. Soc. 2005, 127 (34), 12046–12053. 10.1021/ja0519031. [PubMed: 16117545]

(53). Hadt RG; Sun N; Marshall NM; Hodgson KO; Hedman B; Lu Y; Solomon EI Spectroscopic and DFT Studies of Second-Sphere Variants of the Type 1 Copper Site in Azurin: Covalent and Nonlocal Electrostatic Contributions to Reduction Potentials. J. Am. Chem. Soc. 2012, 134 (40), 16701–16716. 10.1021/ja306438n. [PubMed: 22985400]

(54). Suzuki N; Hofstra JL; Poremba KE; Reisman SE Nickel-Catalyzed Enantioselective Cross-Coupling of N-Hydroxyphthalimide Esters with Vinyl Bromides. Org. Lett. 2017, 19 (8), 2150–2153. 10.1021/acs.orglett.7b00793. [PubMed: 28375631]

(55). Arias-Rotondo DM; McCusker JK The Photophysics of Photoredox Catalysis: A Roadmap for Catalyst Design. Chem. Soc. Rev. 2016, 45 (21), 5803–5820. 10.1039/C6CS00526H. [PubMed: 27711624]

(56). Fillman KL; Przyojski JA; Al-Afyouni MH; Tonzetich ZJ; Neidig ML A Combined Magnetic Circular Dichroism and Density Functional Theory Approach for the Elucidation of Electronic Structure and Bonding in Three- and Four-Coordinate Iron(ii)–N-Heterocyclic Carbene Complexes. Chem. Sci. 2015, 6 (2), 1178–1188. 10.1039/C4SC02791D. [PubMed: 25621143]

(57). Kawamata Y; Vantourout JC; Hickey DP; Bai P; Chen L; Hou Q; Qiao W; Barman K; Edwards MA; Garrido-Castro AF; deGruyter JN; Nakamura H; Knouse K; Qin C; Clay KJ; Bao D; Li C; Starr JT; Garcia-Irizarry C; Sach N; White HS; Neurock M; Minteer SD; Baran PS Electrochemically Driven, Ni-Catalyzed Aryl Amination: Scope, Mechanism, and Applications. J. Am. Chem. Soc. 2019, 141 (15), 6392–6402. 10.1021/jacs.9b01886. [PubMed: 30905151]

(58). Cherney AH Development of Nickel-Catalyzed Asymmetric Reductive Cross-Coupling of Benzylic Electrophiles, California Institute of Technology, 2015. https://resolver.caltech.edu/CaltechTHESIS:06012015-102412340.

(59). Venanzi LM 140. Tetrahedral Nickel(II) Complexes and the Factors Determining Their Formation. Part I. Bistriphenylphosphine Nickel(II) Compounds. J. Chem. Soc. 1958, No. 0, 719–724. 10.1039/JR9580000719.

(60). Garton G; Henn DE; Powell HM; Venanzi LM 682. Tetrahedral Nickel(II) Complexes and the Factors Determining Their Formation. Part V. The Tetrahedral Co-Ordination of Nickel in Dichlorobistriphenylphosphinenickel. J. Chem. Soc. 1963, No. 0, 3625–3629. 10.1039/JR9630003625.

(61). Cotton FA; Goodgame DML New Tetrahedral Complexes of Nickel(II). J. Am. Chem. Soc. 1960, 82 (22), 5771–5774. 10.1021/ja01507a001.

(62). Venanzi LM Tetrahedral Complexes of Nickel (II) and the Factors Determining Their Formation. Journal of Inorganic and Nuclear Chemistry 1958, 8, 137–142. 10.1016/0022-1902(58)80175-X.

(63). Cotton FA; Faut OD; Goodgame DML Preparation, Spectra and Electronic Structures of Tetrahedral Nickel(II) Complexes Containing Triphenylphosphine and Halide Ions as Ligands. J. Am. Chem. Soc. 1961, 83 (2), 344–351. 10.1021/ja01463a021.

(64). Davies JE; Gerloch M; Phillips DJ Phosphine π-Acceptor Properties in Dihalogenobis(Triphenylphosphine)-Nickel(II) and -Cobalt(II). J. Chem. Soc., Dalton Trans. 1979, No. 11, 1836–1842. 10.1039/DT9790001836.

(65). Gerloch M; Hanton LR; Manning MR Tetrahedral Complexes of Nickel(II): Electronic Spectra, γ and π Bonding, and the Electroneutrality Principle. Inorganica Chimica Acta 1981, 48, 205–214. 10.1016/S0020-1693(00)90092-6.

(66). Koester VJ; Dunn TM Electronic Spectrum of the Tetrachloronickelate(II) Complex at 2.2.Deg.K. Inorg. Chem. 1975, 14 (8), 1811–1817. 10.1021/ic50150a014.

(67). Lever AB P. Inorganic Electronic Spectroscopy, 2nd ed.; Elsevier, 1984.

(68). Gerloch M; Manning MR Structural and Ligand Field Parameters of Some Trigonally Distorted Tetrahedral Cobalt(II) and Nickel(II) Complexes. Inorg. Chem. 1981, 20 (4), 1051–1056. 10.1021/ic50218a020.

(69). Sigel H; Martin RB Coordinating Properties of the Amide Bond. Stability and Structure of Metal Ion Complexes of Peptides and Related Ligands. Chem. Rev. 1982, 82 (4), 385–426. 10.1021/cr00050a003.

(70). Connelly NG; Geiger WE Chemical Redox Agents for Organometallic Chemistry. Chem. Rev. 1996, 96 (2), 877–910. 10.1021/cr940053x. [PubMed: 11848774]

(71). Okamoto K; Shida N; Morizumi H; Kitano Y; Chiba K Oxidation Potential Gap (ΔEox): The Hidden Parameter in Redox Chemistry. Angewandte Chemie International Edition 2022, 61 (30), e202206064. 10.1002/anie.202206064. [PubMed: 35610179]

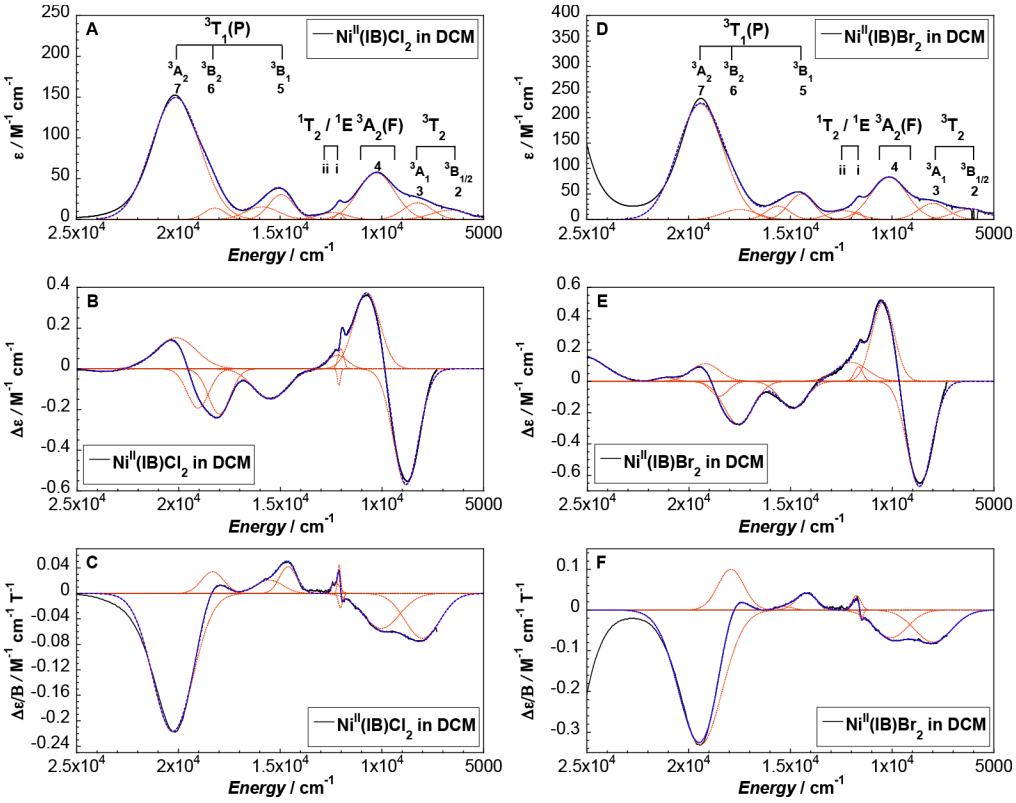

Figure 1.

Spectroscopic characterization of the Ni complexes. Room temperature (**A, D**) UV-vis-NIR absorption, (**B, E**) CD, and (**C, F**) MCD spectra of **$Ni^{II}(IB)Cl_2$** and **$Ni^{II}(IB)Br_2$** in DCM with Gaussian resolutions of individual transitions (orange). Overall fit to each spectrum given in dashed blue.

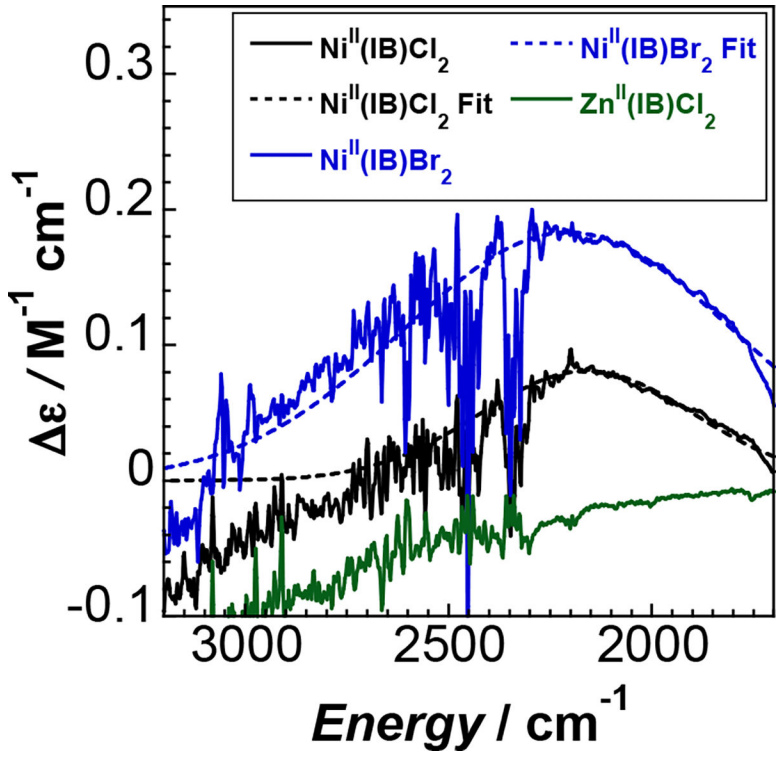

Figure 2.

Background-corrected vibrational CD spectra of 160.0 mM **$Ni^{II}(IB)Cl_2$**, 139.0 mM **$Ni^{II}(IB)Br_2$**, and 115.2 mM **$Zn^{II}(IB)Cl_2$** in d^2-DCM.

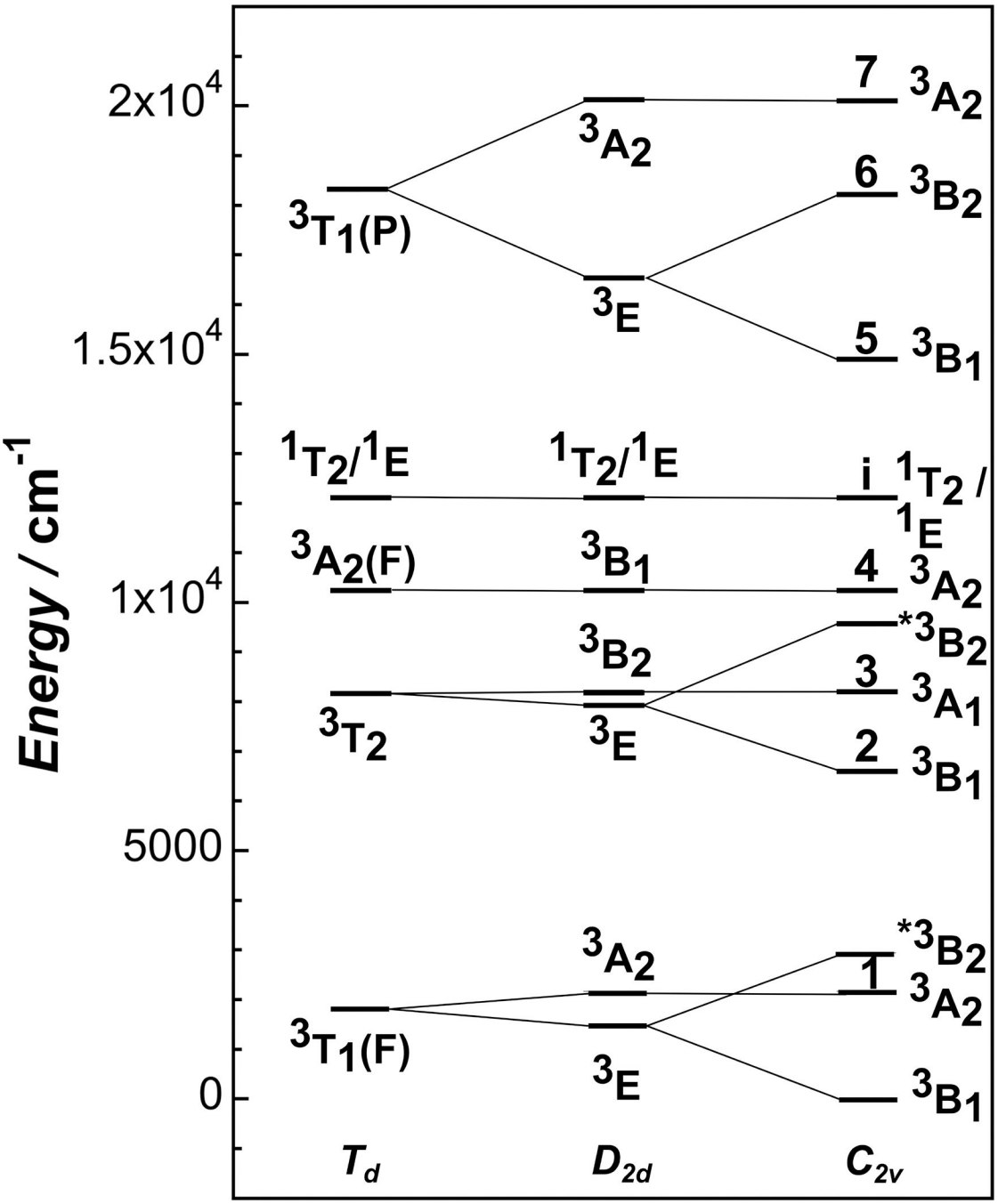

Figure 3.

Descent in symmetry state diagram for $Ni^{II}(IB)Cl_2$. Starred states are derived from CASSCF/CASPT2 calculations and shifted by the average ratio of the seven experimental spin-allowed transitions vs. seven calculated ligand field energies. Numbered states given in Table 1.

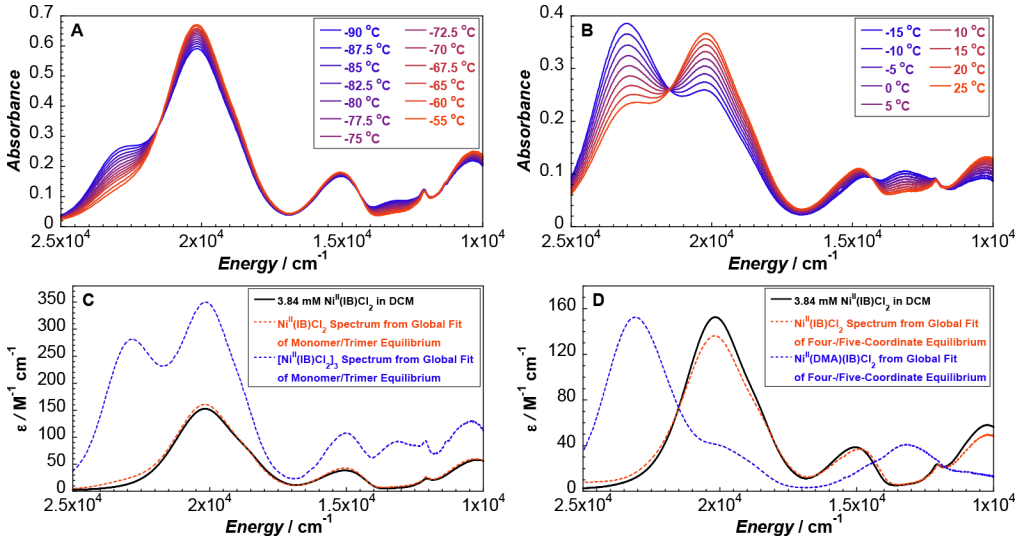

Figure 4.

VT studies of Ni^{II} precatalysts. VT UV-vis-NIR spectra of (**A**) 4.3 mM **$Ni^{II}(IB)Cl_2$** in DCM and (**B**) 3.6 mM **$Ni^{II}(IB)Cl_2$** in DMA, as well as corresponding resolved spectra from global nonlinear regression for (**C**) **$Ni^{II}(IB)Cl_2$** monomer and trimer and (**D**) four- and five-coordinate **$Ni^{II}(IB)Cl_2$** monomer. Note analogous spectra for **$Ni^{II}(IB)Br_2$** are presented in Figures S11–12.

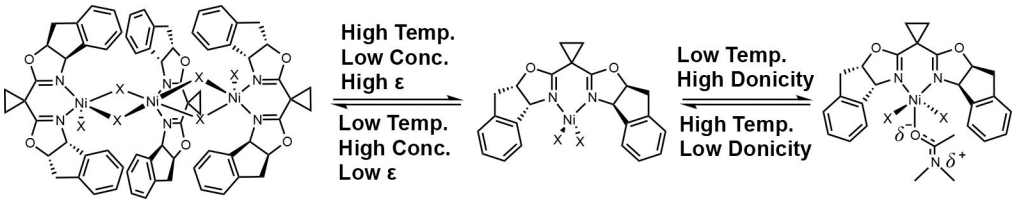

Figure 5.

Equilibrium behavior of **$Ni^{II}(IB)X_2$** based on solvent conditions and concentration. Note while trimerization is not observed for **$Ni^{II}(IB)Br_2$**, it may form at higher concentrations or lower temperatures accessed herein.

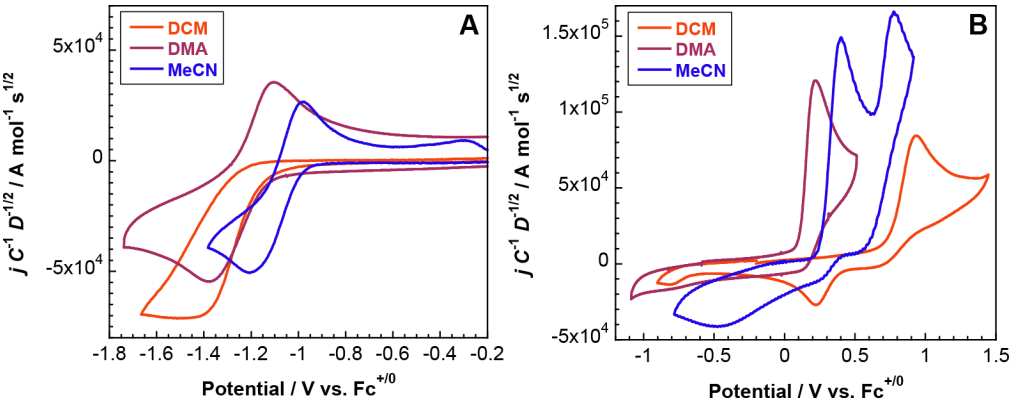

Figure 6.

Solvent-dependent, diffusion- and concentration-normalized voltammetry of **Ni^{II}(IB)Br_2** (details of normalization are provided in Section S5 in the Supporting Information). All electrochemistry acquired in 0.1 M $TBAPF_6$ solution at a scan rate of 100 mV s^{-1}.

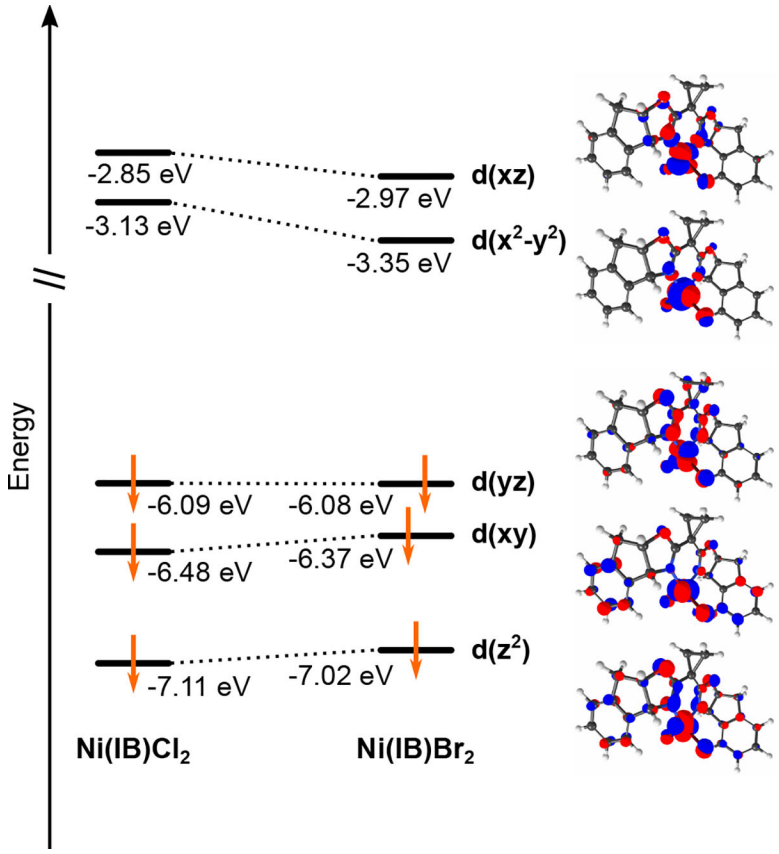

Figure 7.

Comparison between 3d β-orbital manifolds of $\mathbf{Ni^{II}(IB)X_2}$ precatalysts demonstrating the destabilization of the β-LUMOs due to differences in Cl vs. Br ligand field strength.

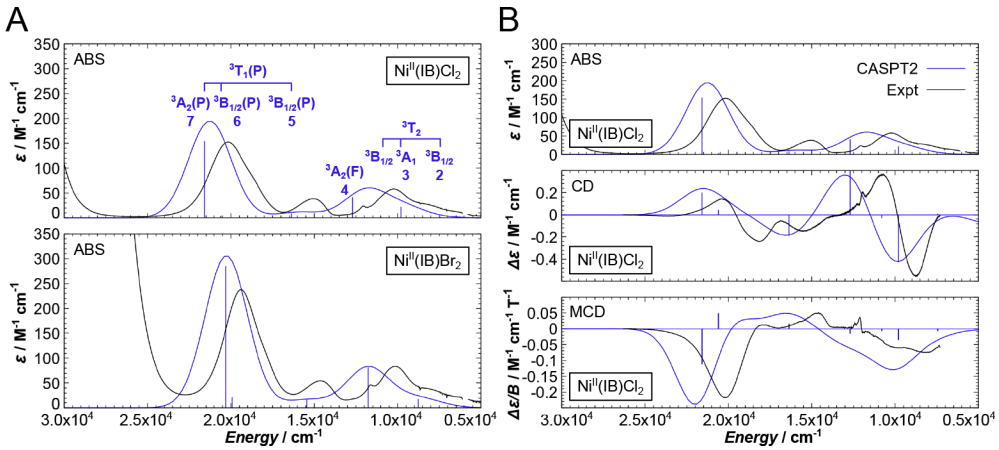

Figure 8.

Comparison between calculated (CASPT2, 22e,12o; blue) and experimental (black) spectra. (**A**) UV-vis-NIR absorption spectra of **$Ni^{II}(IB)Cl_2$** (top) and **$Ni^{II}(IB)Br_2$** (bottom). Group theory assignments are given along with bands numbered as in experiment. The state ordering is the same for **$Ni^{II}(IB)Br_2$**. (**B**) UV-vis-NIR absorption, CD, and MCD spectra of **$Ni^{II}(IB)Cl_2$**. Note absorption and CD spectra are not normalized, while the computed MCD spectrum has normalized intensities to match experiment. Corresponding data for **$Ni^{II}(IB)Br_2$** are presented in Figure S142 in the Supporting Information.

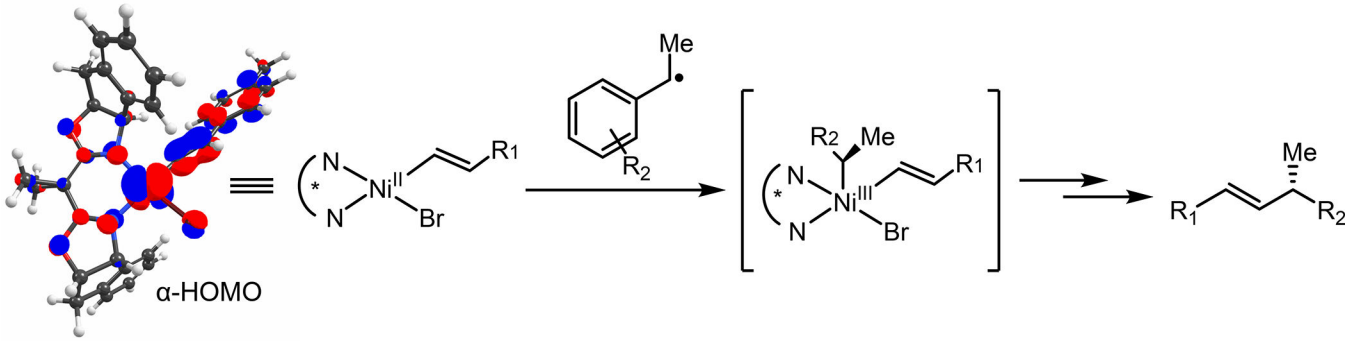

Figure 9.

RAMO of the resting **Ni^{II}(IB)(Vn)X** for the Ni$^{II/III}$ redox couple and radical capture with Vn = 1-methyl-4-vinylbenzene and X = Br.

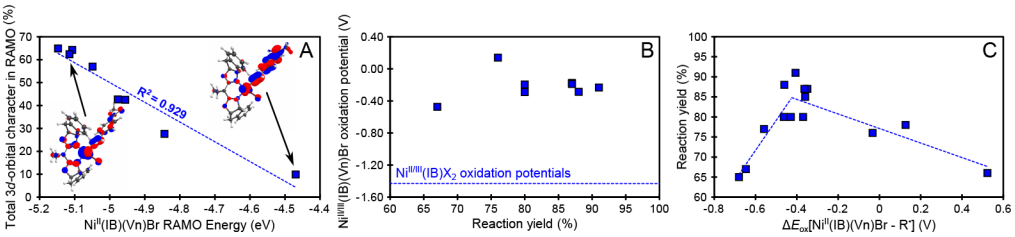

Figure 10.

Electronic structure and reactivity considerations for precatalysts and resting states. (**A**) Correlation between the total 3*d* orbital character in the RAMO of the **Ni^{II}(IB)(Vn)Br** and the RAMO energy. (**B**) Comparison between the **Ni$^{II/III}$(IB)(Vn)Br** oxidation potentials vs. reaction yields of the Vn/ethylbenzene C−C coupling with benzyl-C(sp^3) radicals generated by reduction of NHP esters. Blue line indicates the oxidation potentials of **Ni$^{II/III}$(IB)X$_2$** precatalysts to demonstrate insufficient reactivity to compete with **Ni^{II}(IB)(Vn)Br** to quench benzyl-C(sp^3) radicals. (**C**) Reaction yields of various Vn/benzyl-C(sp^3) C−C coupling reactions plotted against the difference between computed oxidation potentials of **Ni$^{II/III}$(IB)(Vn)Br** and benzyl-C(sp^3) radicals. Note all values are also tabulated in Table S8. Reaction yields plotted from Reference 54.

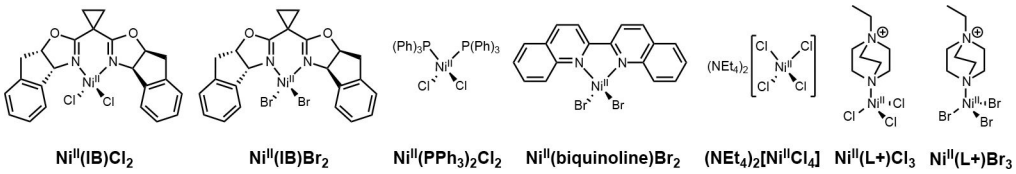

Figure 11.
Structures of pseudo-T_d Ni^{II} complexes used for comparison in Table 6.

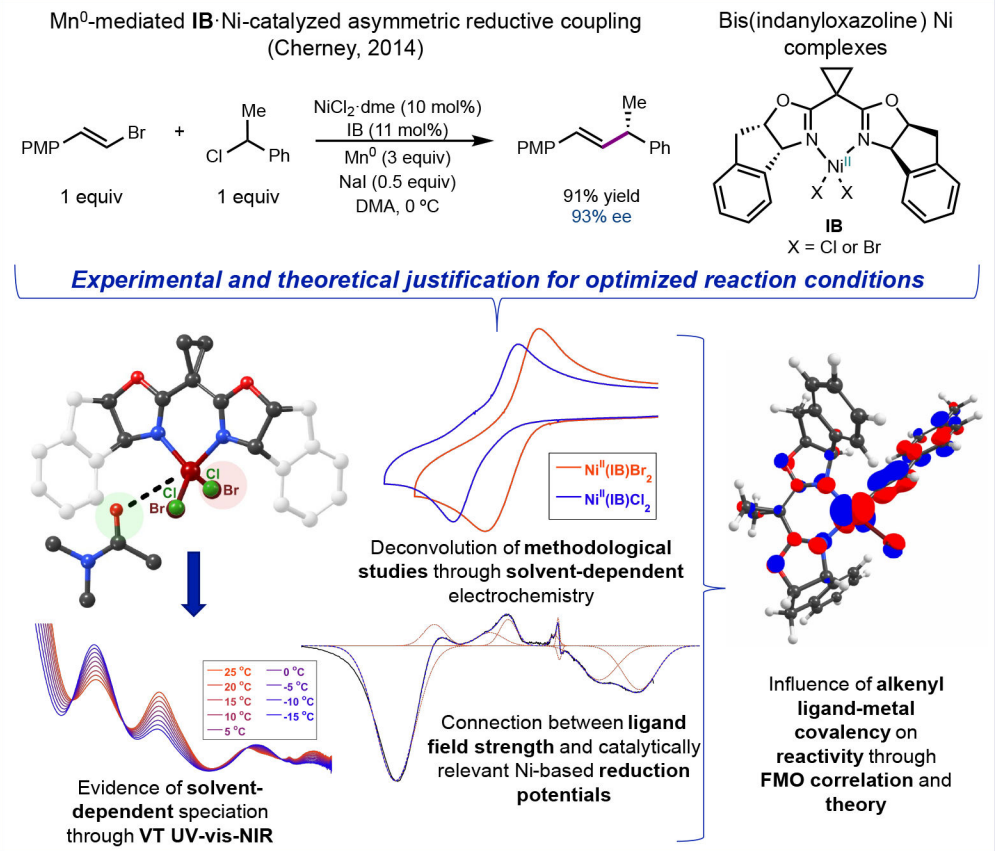

Scheme 1.

Outline of key findings from this comprehensive spectroscopic, electrochemical, and computational study of Ni^{II} precatalysts for enantioselective reductive alkenylation. FMO = frontier molecular orbital.

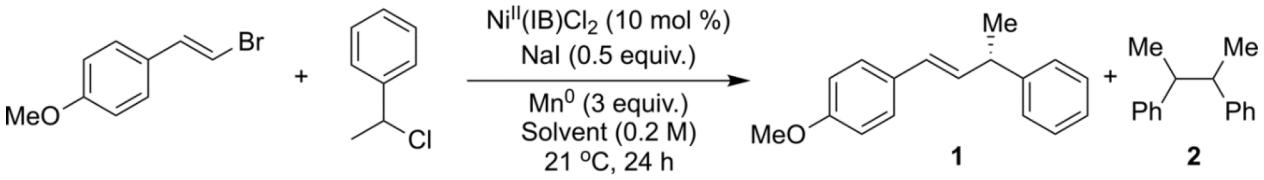

Solvent	Donor Number (kcal mol^{-1}) (BF_3 Affinity)	Acceptor Number	Yield of 1	Ratio of Yields for 1 to 2
N-Methyl-2-pyrrolidone (NMP)	26.9	13.3	52% ± 1%	2.1
N,N'-Dimethylpropyleneurea (DMPU)	26.8	---	38% ± 1%	1.2
N,N'-Dimethylacetamide (DMA)	26.8	13.6	72% ± 2%	4.1
N'N'-Dimethylformamide (DMF)	26.4	16.0	50% ± 2%	1.6
Tetrahydrofuran (THF)	21.6	8.0	30% ± 1%	0.9
Ethyl Acetate (EtOAc)	18.1	9.3	33% ± 3%	1.1
1,2-Dimethoxyethane (DME)	17.8	10.2	34% ± 2%	1.1
1,4-Dioxane	17.7	10.8	---	---
Acetonitrile (MeCN)	14.4	18.9	16% ± 1%	0.4
Dichloromethane (DCM)	2.4	20.4	---	---

Scheme 2.

Conversion and cross-coupled yields for a representative reductive cross-coupling of (1-chloroethyl)benzene and (*E*)-1-(2-bromovinyl)-4-methoxybenzene using **Ni^{II}(IB)Cl$_2$**, along with donor and acceptor numbers for solvents tested in optimization studies. Standard errors were calculated from three trials. Experimental procedure given in Supporting Information Section S1. D-BF_3 donor numbers taken from References 32 and 33. Acceptor numbers (ANs) taken from Reference 33. All ANs measured with respect to the affinity of antimony pentachloride towards triethylphosphine oxide.

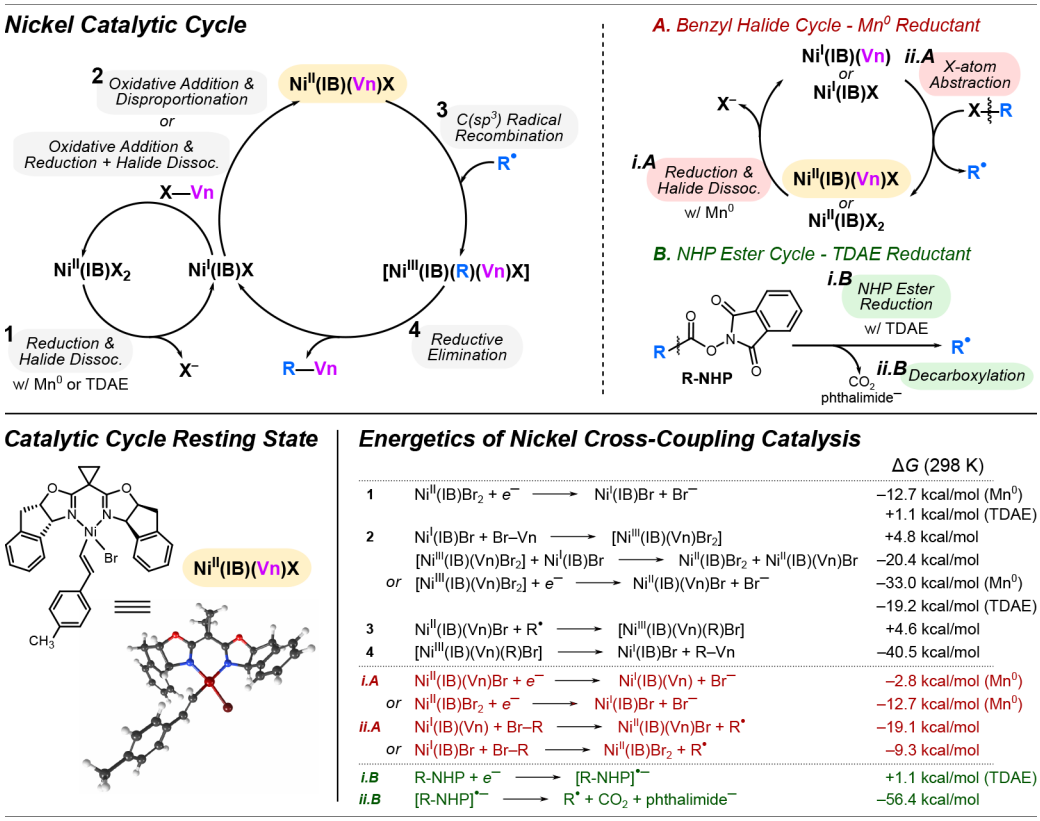

Scheme 3.

Representative computed $Ni^{I/III}$ catalytic cycle for the cross-coupling of $C(sp^2)$ vinyl and $C(sp^3)$ benzyl electrophiles. Relative Gibbs free energy values were computed at the TPSSh (CPCM) level for X = Br. Reactions involving electron transfers were corrected by adding the energy of $Mn^{0/2+}$ redox couple or $TDAE^{0/+}$, which were used as the external reducing agents in refs. [54] and [7]. Note that we have adopted values of E^{o} = −1.94 V vs. $Fc^{+/0}$ for $Mn^{2+/0}$ obtained from the experiments in refs. [48] and [70] and E^{o} = −1.34 V vs. $Fc^{+/0}$ for $TDAE^{+/0}$ from computations in this article.

Table 1.

Band maxima and full widths at half maxima (FWHM) for **$Ni^{II}(IB)Cl_2$** and **$Ni^{II}(IB)Br_2$** in DCM obtained from simultaneous Gaussian resolution of UV-vis-NIR, CD, MCD, and vibrational CD spectra. Numbered states correspond to spin-allowed ligand field transitions.

$Ni^{II}(IB)Cl_2$							
	Absorption (cm^{-1})		**CD (cm^{-1})**		**MCD (cm^{-1})**		**Assignment**
#	**Band max.**	**FWHM**	**Band max. (Sign)**	**FWHM**	**Band max. (Sign)**	**FWHM**	***T_d*: *C_{2v}* Geometry**
1	---	---	2170 (+)	730	---	---	$^3T_1(F)$: $^3B_1(F) \rightarrow {}^3A_2(F)$
2	6640	2160	---	---	---	---	$^3T_2$: $^3B_1(F) \rightarrow {}^3B_1/{}^3B_2$
3	8240	1680	8820 (−)	1480	8010 (−)	2000	$^3T_2$: $^3B_1(F) \rightarrow {}^3A_1$
4	10 270	2110	10 750 (+)	1500	10 030 (−)	2110	$^3A_2(F)$: $^3B_1(F) \rightarrow {}^3A_2(F)$
i	12 100	400	12 020 (+)	330	12 030 (−)	250	$^3B_1(F) \rightarrow {}^1T_2/{}^1E$
	---	---	12 120 (−)	180	12 100 (+)	170	$^3B_1(F) \rightarrow {}^1T_2/{}^1E$
ii	12 400	1630	12 200 (+)	1150	---	---	Spin-forbidden LF
5	14 940	1430	---	---	14 610 (+)	1000	$^3T_1(P)$: $^3B_1(F) \rightarrow {}^3B_1(P)$
iii	15 890	1910	15 500 (−)	1950	15 530 (+)	1570	---
6	18 210	1220	18 000 (−)	1250	18 320 (+)	1280	$^3T_1(P)$: $^3B_1(F) \rightarrow {}^3B_2(P)$
iv	---	---	19 050 (−)	1250	---	---	---
7	20 130	2800	20 130 (+)	2300	20 270 (−)	2330	$^3T_1(P)$: $^3B_1(F) \rightarrow {}^3A_2(P)$
v	---	---	23 740 (−)	1600	---	---	LF of Trimer
$Ni^{II}(IB)Br_2$							
	Absorption (cm^{-1})		**CD (cm^{-1})**		**MCD (cm^{-1})**		**Assignment**
#	**Band max.**	**FWHM**	**Band max. (Sign)**	**FWHM**	**Band max. (Sign)**	**FWHM**	***T_d*: *C_{2v}* Geometry**
1	---	---	2210 (+)	970	---	---	$^3T_1(F)$: $^3B_1(F) \rightarrow {}^3A_2(F)$
2	6150	2000	---	---	---	---	$^3T_2$: $^3B_1(F) \rightarrow {}^3B_1/{}^3B_2$
3	7980	1670	8670 (−)	1450	7980 (−)	2150	$^3T_2$: $^3B_1(F) \rightarrow {}^3A_1$
4	10 150	2080	10 460 (+)	1280	10 060 (−)	1930	$^3A_2(F)$: $^3B_1(F) \rightarrow {}^3A_2(F)$
	---	---	---	---	11 500 (−)	180	$^3B_1(F) \rightarrow {}^1T_2/{}^1E$
i	11 670	500	11 660 (+)	500	11 750 (+)	500	$^3B_1(F) \rightarrow {}^1T_2/{}^1E$
ii	12 380	1750	12 000 (+)	1830	---	---	Spin-forbidden LF
5	14 460	1450	14 900 (−)	1530	14 210 (+)	1280	$^3T_1(P)$: $^3B_1(F) \rightarrow {}^3B_1(P)$
iii	15 600	1330	---	---	15 290 (+)	970	---
6	17 500	2000	17 560 (−)	1650	17 920 (+)	1500	$^3T_1(P)$: $^3B_1(F) \rightarrow {}^3B_2(P)$
iv	---	---	18 500 (−)	1030	---	---	---
7	19 410	2660	19 200 (+)	1670	19 420 (−)	2500	$^3T_1(P)$: $^3B_1(F) \rightarrow {}^3A_2(P)$
v	---	---	21 130 (+)	1030	---	---	$^3B_1(F) \rightarrow {}^1T_{1g}, {}^1T_{2g}, {}^1A_{1g}, {}^1E_g$

vi	---	---	25 100 (+)	2400	---	---	LMCT

Table 2.

Thermodynamic reaction parameters for transition metal oligomers and solvent adducts of $\mathbf{Ni^{II}(IB)X_2}$ species. 95% confidence intervals of global fitting given in brackets.

Complex	Standard Enthalpy [Range]	Standard Entropy [Range]	Free Energy (294 K)	K_{eq} (294 K)
$\mathbf{Ni^{II}(IB)(DMA)Cl_2}$	−5.0 kcal mol^{-1} [−4.3, −7.1]	−18.1 cal mol^{-1} K^{-1} [−15.4, −25.1]	0.3 kcal mol^{-1}	0.58
$\mathbf{Ni^{II}(IB)(DMA)Br_2}$	−6.1 kcal mol^{-1} [−4.2, −8.3]	−20.8 cal mol^{-1} K^{-1} [−13.4, −28.9]	0.02 kcal mol^{-1}	0.97
$\mathbf{[Ni^{II}(IB)Cl_2]_3}$	−8.2 kcal mol^{-1} [−4.1, −12.5]	−22.3 cal mol^{-1} K^{-1} [−1.5, −43.7]	−1.6 kcal mol^{-1}	16.7

Table 3.

Electrochemical parameters for **$Ni^{II}(IB)Cl_2$** and **$Ni^{II}(IB)Br_2$** in 0.1 M $TBAPF_6$ electrolyte solution using a glassy carbon working electrode, 0.01 M $Ag^{+/0}$ non-aqueous reference electrode, and platinum wire counter electrode. All peak and formal potentials are given in volts, obtained using a 100 mV s^{-1} scan rate (unless otherwise stated), and referenced to $Fc^{+/0}$.

Complex	Solvent	$E_{p,a,1}$	$E_{p,a,2}$	$E_{p,c}$	$E_{p/2,c}$	$E_c^{0'}$ [a]	$E_a^{0'}$ [a]	D_0 (cm^2 s^{-1}) [b]
$Ni^{II}(IB)Cl_2$	DCM	1.51 [d]	---	−1.58	−1.44	−1.47	1.38 [d]	9.25×10^{-6}
$Ni^{II}(IB)Br_2$	DCM	0.94	---	−1.46	−1.26	−1.26	0.85	9.25×10^{-6}
$Ni^{II}(IB)Cl_2$	MeCN	0.96	---	−1.46	−1.25	−1.32	0.81	1.05×10^{-5}
$Ni^{II}(IB)Br_2$	MeCN	0.36	0.75	−1.21	−1.07	−1.05	0.30/0.67	9.55×10^{-6}
$Ni^{II}(IB)Cl_2$	DMA	0.67 [e]	---	−1.54	−1.42	−1.47	0.48	2.81×10^{-6}
$Ni^{II}(IB)Br_2$	DMA	0.22	---	−1.37	−1.23	−1.23	0.15	3.06×10^{-6}
$Ni^{II}(^{diBn}biOx)Br_2$ [c]	1,2-DFB	---	---	−1.90	−1.55	---	---	---
$Ni^{II}(^{iPr}biOx)Br_2$ [c]	1,2-DFB	---	---	−1.64	−1.46	---	---	---
$Ni^{II}(^{diMe}biOx)(Dipp)Br$ [c]	THF	---	---	−2.39	−2.12	---	---	---

[a] From the inflection potential of the redox process at 100 mV s^{-1}, which approximates the formal potential.

[b] Derived from mass transport-controlled current at a disk microelectrode.

[c] See reference 40.

[d] Estimated from the local minimum of dj/dV at 25 mV s^{-1}.

[e] Estimated from the local minimum of dj/dV at 100 mV s^{-1}.

$E_{p/2,c}$ is the potential at half of the peak current.

Table 4.

Experimental (UV-vis-NIR absorption) and predicted electronic transition energies for **$Ni^{II}(IB)Cl_2$** and **$Ni^{II}(IB)Br_2$**.

Predicted transition energies (cm^{-1})						Assignment, (#)[b]
$Ni(IB)Cl_2$			$Ni(IB)Br_2$			
Experiment	*DFT*	*CASPT2*	*Experiment*	*DFT*	*CASPT2*	
2170[a]	7629	2009	2210[a]	7242	1824	$^3T_1(F)$: $^3B_1(F) \rightarrow A_2(F)$, (1)
---	10 056	3318	---	9730	2974	$^3T_2$: $^3B_1(F) \rightarrow {}^3B_1/{}^3B_2$
6640	14 393	7443	6150	13 924	7229	$^3T_2$: $^3B_1(F) \rightarrow {}^3B_1/{}^3B_2$, (2)
8240	14 991	9786	7980	14 972	9322	$^3T_2$: $^3B_1(F) \rightarrow {}^3A_1$, (3)
---	---	10 810	---	---	10 244	$^3T_2$: $^3B_1(F) \rightarrow {}^3B_1/{}^3B_2$
10 270	---	12 709	10 150	---	12 382	$^3A_2(F)$: $^3B_1(F) \rightarrow {}^3A_2(F)$, (4)
14 940	18 462	16 354	14 460	17 529	16 112	$^3T_1(P)$: $^3B_1(F) \rightarrow {}^3B_1(P)$, (5)
18 210	---	20 607	17 500	---	19 514	$^3T_1(P)$: $^3B_1(F) \rightarrow {}^3B_2(P)$, (6)
20 130	17 166	21 586	19 410	16 834	19 561	$^3T_1(P)$: $^3B_1(F) \rightarrow {}^3A_2(P)$, (7)

[a] Experimental energies for the $^3B_1(F) \rightarrow A_2(F)$ band were taken from the VCD spectroscopy.

[b] Numbered states correspond to spin-allowed ligand field transitions observed in experiments.

Table 5.

Computed formal potentials for **$Ni^{II}(IB)Cl_2$** and **$Ni^{II}(IB)Br_2$**. All potentials referenced to $Fc^{+/0}$ with computed absolute potential of –4.55 eV to compare the effect of solvent coordination without the shift induced by $Fc^{+/0}$ in different solvents. Note that MeCN and DMA are essentially indistinguishable in the CPCM and produce the same computed value of $Fc^{+/0}$ absolute potential.

Coordinated Solvent	Reaction	V vs. $Fc^{+/0}$
None	$Ni^{II}(IB)Cl_2 + e^- \rightarrow Ni^{I}(IB)Cl_2$	−1.24
	$Ni^{II}(IB)Cl + e^- \rightarrow Ni^{I}(IB)Cl$	−0.20
	$Ni^{II}(IB)Cl_2 + e^- \rightarrow Ni^{I}(IB)Cl + Cl^-$	−1.49
	$Ni^{II}Ni^{I}(IB)_2Cl_4$ Dimer + $e^- \rightarrow [Ni^{I}(IB)Cl_2]_2$ Dimer	−1.28
	$Ni^{II}(IB)Br_2 + e^- \rightarrow Ni^{I}(IB)Br_2$	−1.11
	$Ni^{II}(IB)Br + e^- \rightarrow Ni^{I}(IB)Br$	−0.13
	$Ni^{II}(IB)Br_2 + e^- \rightarrow Ni^{I}(IB)Br + Br^-$	−1.39
	$Ni^{II}Ni^{I}(IB)_2Br_4$ Dimer + $e^- \rightarrow [Ni^{I}(IB)Br_2]_2$ Dimer	−1.26
MeCN	$Ni^{II}(IB)Cl(MeCN) + e^- \rightarrow Ni^{I}(IB)Cl(MeCN)$	−0.59
	$Ni^{II}(IB)Cl_2(MeCN) + e^- \rightarrow Ni^{I}(IB)Cl(MeCN) + Cl^-$	−1.65
	$Ni^{II}(IB)Cl_2(MeCN) + e^- \rightarrow Ni^{I}(IB)Cl_2 + MeCN$	−1.03
	$Ni^{II}(IB)Br(MeCN) + e^- \rightarrow Ni^{I}(IB)Br(MeCN)$	−0.90
	$Ni^{II}(IB)Br_2(MeCN) + e^- \rightarrow Ni^{I}(IB)Br(MeCN) + Br^-$	−1.48
	$Ni^{II}(IB)Br_2(MeCN) + e^- \rightarrow Ni^{I}(IB)Br_2 + MeCN$	−0.85
DMA	$Ni^{II}(IB)Cl(DMA) + e^- \rightarrow Ni^{I}(IB)Cl(DMA)$	−1.17
	$Ni^{II}(IB)Cl_2(DMA) + e^- \rightarrow Ni^{I}(IB)Cl(DMA) + Cl^-$	−1.66
	$Ni^{II}(IB)Cl_2(DMA) + e^- \rightarrow Ni^{I}(IB)Cl_2 + DMA$	−1.06
	$Ni^{II}(IB)Br(DMA) + e^- \rightarrow Ni^{I}(IB)Br(DMA)$	−1.09
	$Ni^{II}(IB)Br_2(DMA) + e^- \rightarrow Ni^{I}(IB)Br(DMA) + Br^-$	−1.44
	$Ni^{II}(IB)Br_2(DMA) + e^- \rightarrow Ni^{I}(IB)Br_2 + DMA$	−0.86

Table 6.

Comparison between spin-allowed transition energies for **$Ni^{II}(IB)Cl_2$** and **$Ni^{II}(IB)Br_2$** in DCM and previously studied pseudo-T_d Ni^{II} complexes (units of cm^{-1}).

Complex	$^3B_1(F) \rightarrow {}^3A_2(F)$	$^3B_1(F) \rightarrow {}^3B_1/{}^3B_2(F)$	$^3B_1(F) \rightarrow {}^3A_1(F)$	$^3B_1(F) \rightarrow {}^3A_2(F)$	$^3B_1(F) \rightarrow {}^3B_1(P)$	$^3B_1(F) \rightarrow {}^3B_2(P)$	$^3B_1(F) \rightarrow {}^3A_2(P)$
$Ni^{II}(IB)Cl_2$ [a]	2170	6640	8240	10 270	14 940	18 210	20 130
$Ni^{II}(IB)Br_2$ [a]	2210	6140	7970	10 140	14 570	17 420	19 380
$Ni^{II}(PPh_3)_2Cl_2$ [b]	4500	10 200	8000	11 200	18 100	14 600 – 16 400*	17 600
Ni^{II}(biquinoline)Br_2 [c]	3740	4941	6020	9810	18 450	17 300	19 430
$[Ni^{II}Cl_4]$ 2- [d]	4440	3970	4440	6870	14 250	14 250	15 240
$Ni^{II}(L+)Cl_3$ [e]	4660*	5260	6410	9090	16 000	16 000	17 240
$Ni^{II}(L+)Br_3$ [e]	4530	5100	6410	8700	15 200 – 16 100	15 200 – 16 100	16 250

[a] This work.

[b] Reference 64.

[c] Reference 65.

[d] References 66 and 67.

[e] Reference 68.

Starred transition energies are obtained from crystal field analysis of other experimentally observed transitions.